Photodegradation of Toxaphene and Tetradifon Insecticides Using Novel Au Nanoparticles/CdSe/WO_3 Nanocomposite

DELİA TERESA SPONZA, RUKİYE ÖZTEKİN*
Department of Environmental Engineering
Dokuz Eylül University
Tınaztepe Campus, 35160 Buca/Izmir,
TURKEY

**Corresponding Author*

Abstract: - A new nanocomposite namely gold nanoparticles doped cadmium selenium doped tungsten trioxide (Au/CdSe/WO3) photocatalyst was produced under laboratory conditions to photodegrade the toxaphene and tetradifon insecticides from a chemical industry wastewaters producing insecticides. The XRD pathways of WO3 exhibited that it displays a number of peaks at 2θ = 25.09o, 24.63o, 25.60o, 27.09o, 29.09o, 34.011o, 35.99o, 42.86o, 53.40o. FTIR results showed that the band at 976 cm−1 signifies the W = O stretching vibration whereas the band appearing at 1396 cm−1 corroborated to the O–H bending vibration in W–OH. TEM data showed that Au/CdSe/WO3 nanocomposite consisting of Au, CdSe and WO3. Bare WO3 exhibited irregular/non-spherical nano-beads while the CdSe has sheets in huge density with packed sheets . The surface plasmon resonance (SPR) peak at around 590 nm confirms the transformation of Au/CdSe/WO3 nanomaterials to plasmonic Au/CdSe/WO3 nanocomposite. The XPS peak at 288.12 eV signifies the existence of oxygenated functional groups such as C-O, C O, or COOH within nanocomposite, resulting from oxidation of carbon. The bandgap values of nanocomposite calculated with Kubelka-Munk function are 3.05 eV, 3.15 eV and 3.16 eV at 500°C, 650°C and 800°C temperatures,respectively. For maximum toxaphene (99%) and tetradifon (97%) photodegradation yields the optimized operational conditions were as follows: 800 mg/l insecticide concentration, 20oC temperature, 1 mg/l Au/CdSe/WO3 nanocomposite dose, pH=8.0, 10 min retention time and a light power of 20 W/m2. The reusability of the Au/CdSe/WO3 nanocomposite was performed during 80 cycles. From the 1st to the 79th cycle, the photodegradation efficiencies for both toxaphene and tetradifon were consistently recorded as 99%.

Key-Words: - Chemical industry wastewater; Gold doped cadmium selenide doped tungstene trioxide (Au/CdSe/WO3); Insecticide; Kubelka-Munk function; Nanocomposite; Nanoparticle; Photocatalyst; Photodegradation; Tetradifon; Toxaphene.

Received: December 11, 2025. Revised: February 16, 2026. Accepted: March 12, 2026. Published: June 26, 2026.

1 Introduction

The insecticide usage in farms, their residual limits, and maximum residue limits are strictly regulated by governmental organizations owing to their potential toxicity. Oxidative treatments using ultraviolet (UV) radiation or ozone treatment are generally considered as alternative treatments for use in the post-harvest process, [1], [2]. The absorption of UV and visible light of insecticide molecules activates the nonbonding and bonding electrons in the pollutant molecule and spontaneously initiates the oxidative reaction with oxygen and water in the presence of atmospheric air. In particular, vacuum ultraviolet (VUV, < 200 nm) treatment can be activated the electrons of covalent bonds in oxygen molecules (O_2) and generate ozone (O_3), hydroxide (OH), hydrogen peroxide (H_2O_2), singlet oxygen ($^1O_2$), and other reactive oxygen species (ROS) in air, [3], [4]. These oxidative treatments that occur in air can stimulate the oxidative degradation and decomposition of organic compounds, including pesticides and insecticides, [5]. Recently, the effects of UV irradiation on insecticide residue reduction were studied on several commercial pesticides. O_3 treatments were studied for Pyrethroid, Spinosyn, Pyrazole, Formamidine and Dinitrophenol insecticides, [4], [5].

UV treatment is effective only in the degradation of insecticides residues that are present on the surface of insects, while the degradation capability of O_3 is restricted to certain types of insecticides, [5]. Furthermore, O_3 is retained in the processed crops after the aqueous O_3 treatment. Thus, some stable insecticides resistant to oxidation and UV radiation,

require higher degradation power for removing the residues, [4], [5].

An advanced oxidation process (AOP) was recently applied to wastewater treatment to remove organic contaminants and was known as a more potent oxidative treatment than O_3 or UV. This is a combined treatment with an oxidant (O_3, O_2, and H_2O_2) and a radical initiator [UV, ultrasound, iron ions (Fe^{2+}), titanium dioxide (TiO_2), and alkaline] in aqueous conditions, [5], [6]. Thus, this process can be considered the post-harvest treatment for crops, at the washing step; however, this process is not commonly used because it would create O_3 residue, decrease the crop quality, and increase the exposure risk of ROS to workers, [7]. However, the photochemical AOP, combined with UV may be feasible for use in the drying step in a closed chamber, without concerns of O_3 residue.

Toxaphene is a mixture of more than 177, 10-carbon polychlorinated derivatives. These materials persist in the soil, though not as long as the cyclodienes, and disappear from the surfaces of plants in 3-4 weeks. This disappearance is attributed to more volatility than to photolysis. Toxaphene is rather easily metabolized by mammals and birds, and is not stored in body fat nearly to the extent of dichloro-diphenyl-trichloroethane (DDT), hexachlorocyclohexane (HCH), and the cyclodienes, [1]. Toxaphene was one of the most heavily used pesticides in the United States of America (USA) in the 1970s and early 1980s. It was used primarily to control insect pests on cotton and other crops in the southern USA. Other uses included controlling insect pests on livestock and killing unwanted fish in lakes. Toxaphene was banned for all registered uses by 1990. Toxaphene is made by reacting chlorine gas [Cl_2(g)] with a substance called camphene. The resulting product (toxaphene) is a mixture of hundreds of different chlorinated camphene's and related chemicals, [1]. The chemical structure of toxaphene is illustrated in Figure 1.

* Figure 1 can be found in the Appendix section.

Toxaphene, also known as camphechlor, is a complex compound composed of polychlorinated bornanes (CHBs) and various camphenes. It was formerly one among the most widely used chlorinated pesticides on the planet, with total quantities used estimated in mega tonnes, [1]. It was primarily a commercial product that was popularized for use in agricultural and as animal insecticides, but it was later designated as a persistent pollutant by the Stockholm Convention. Toxaphene has been demonstrated to travel large distances and is considered a common environmental pollutant. It has been demonstrated that like other organochlorine insecticides, it bioaccumulates in aquatic creatures, [1]. There is minimal information on toxaphene in animal feed; however, it has been linked to fish and shellfish products. Toxaphene is a recognized endocrine disruptor and a likely carcinogen, according to toxicological evidence. As a result, this chapter emphasizes the issues faced by toxaphene contamination as well as the many proactive ways that address its consequences, [1].

Tetradifon is a sulfone that is diphenyl sulfone in which one of the phenyl groups is substituted by chlorine at position 4, while the other is substituted by a chlorine at positions 2, 4, and 5. It is an organochlorine acaricide, a trichlorobenzene, a sulfone and a member of mono chlorobenzenes, [2]. Tetradifon is a broad-spectrum organochlorine insecticide and an inhibitor of the mitochondrial oligomycin sensitivity conferring protein (OSCP), which can be used to control a variety of mites (Figure 2). Tetradifon inhibits energy-related activities such as adenosine 5'-diphosphate (ADP)-stimulated respiration, dinitrophenol (DNP) and magnesium ions (Mg^{2+}) stimulated adenosine 5'-triphosphatase (ATPase), with a half maximal inhibitory concentration (IC_{50}) of 4.5-27 nmol/mg mitochondrial protein, [2]. Tetradifon exerts oligomycin-like activity by inhibiting the oxidative phosphorylation process, inducing oxidative stress and interfering with bone metabolism. Tetradifon is currently mainly used in the research of mitochondrial function regulation, bone remodeling mechanism and nephrotoxicity of environmental pollutants, [2].

* Figure 2 can be found in the Appendix section.

Tetradifon pesticide residues from the lemon, orange and grapefruit matrices were achieved by ozonation. All of chlorothalonil residues adsorbed onto the orange matrix and they were completely removed after 5 min ozonation. The highest removal percentages of tetradifon were achieved as 68.60% for the lemon and grapefruit matrices. All of diffused chlorothalonil and chlorpyrifos-ethyl residues were completely removed from both orange and grapefruit matrices after 5 min ozonation. Increasing of applied O_3 dosage was not significantly affect the removal percentages of pesticides whereas increasing of ozonation temperature caused a negative effect on the removal percentages of pesticides, [2].

The reductive dechlorination of 2,2,5-endo,6-exo,8,9,10-heptachlorobornane which is a significant component of the chlorinated insecticide toxaphene was studied using chemical, photochemical, and biological systems, [3]. Findings suggest that the

although, heptachlorobornane undergoes rapid dechlorination, low biological (65%), chemical (49%) and photochemical (62%) yields was detected with O_3 and TiO_2 NCs, [3].

The photocatalytic activity of Mn doped TiO_2 for the ozonation of tetradifon pesticide in aqueous solution was studied. Various loadings of catalysts Mn/TiO_2 (1%, 2.5% and 5%) were prepared and photocatalyzed ozonation with 2.5% Mn/TiO_2 yielded 76% degradation and mineralization of tetradifon in 10 h under basic pH conditions, [4].

Li and Jin, (2013), found that the degradation levels of toxaphene are much higher in May than in January because of increased concentrations of OH primarily due to increased solar radiation. Bartoš et. al., (2005) investigated the transformation of toxaphene in hexane under UV-light conditions in anaerobic soil and sediment. Exposure of toxaphene to UV-irradiation results in dechlorination and dehydrochlorination, mainly of the highly chlorinated congeners. This reaction leads to the formation of chlorobornanes that also degrade in the presence of UV-radiation or by reaction with ROS. UV-radiation contributes to toxaphene photolysis with yields varying between 60% and 70%. Ye et al., (2024), investigated the tetradifon photolysis. The formation of key transient intermediates, such as the corresponding radical cation, radical anion as well as hydrated electron (e_{aq}^-) with low yields (65%). Ye et al., (2024) found low photodegradation yields for toxaphene with sun light (69%) and ozon (72%) applications van Bavel et al., (2003), researched the degradation of toxaphene in water with two kinds of bioreactors under anaerobic conditions and suspended carrier biofilm reactor. After 6 weeks approximately 80% of the total toxaphene was degraded in the anaerobic reactor. The concentrations of toxaphene isomers decreased rapidly with less chlorine substituentls.Thomas et al., (2005), found that the toxaphene photodegradation yields were low under UV (64%) and sun (69%) ligths. Lacayor et al., (2003), found the accumulation of toxaphene and its persistence in the environment in the aquatic food chain and its toxicity to higher animals, and low biodegradability. The recalcitrance of the individual toxaphene components is obviously related to the number, and especially, the position of the Cl_2 substituents. Fenoll et al., (2015), investigated the photocatalytic degradation of three neonicotinoid insecticides namely thiamethoxam and toxaphene in pure water using zinc oxide (ZnO) and TiO_2 as photocatalysts under natural sunlight and artificial light irradiation. The complete disappearance of all the studied compounds was achieved after 60 and 90 min of artificial light irradiation, in the $ZnO/Na_2S_2O_8$ and $TiO_2/Na_2S_2O_8$ systems, respectively.

Limited studies were detected in the literature relevant to photodegradation of toxaphene with nanocomposites. Maddila et al., (2016), researched the photocatalytic activity of Mn doped TiO_2 for the ozonation of tetradifon pesticide in aqueous solution. Various loadings of catalysts Mn/TiO_2 (1%, 2.5% and 5%) was prepared. Photocatalyzed ozonation with 2.5% Mn/TiO_2 yielded 87% degradation and mineralization of tetradifon in 2.0 h under basic pH conditions. For 10 mg/l of tetradifon, 0.1 g/l of catalyst was found to be the optimum for effective mineralisation. Ormad et al., (2010), investigated the influence of H_2O_2 and TiO_2 in the O_3-based treatment to degrade 44 organic pesticides present in natural water, including heptachlor, heptachlor epoxide A, tetradifon and trifluralin. The ozonation using 3 mgO_3/l produces a pesticides removal close to 23%, whereas the application of O_3/H_2O_2 and O_3/TiO_2 treatments achieves average degradation yields lower than the ozonation. However, the application of $O_3/H_2O_2/TiO_2$ process improves considerably the pesticides degradation and an average degradation yield of 36%. Araña et al., (2008), investigated the photocatalytic and biological degradation of two mixtures of and two fungicides. The photocatalytic method was able to degrade dicofol, tetradifon, pyrimethanil and the components of Ronstar herbicides. The proper dosage of the water containing the pesticides to a photocatalytic reactor followed by a wetland reactor resulted to be the most successful strategy for the detoxification of the studied compounds and their mixtures.

Semiconductors are among the most efficient materials for photocatalytic degradation. They are capable of generating ROS with high oxidation potentials—hydroxyl radicals, $OH^{\bullet}$; superoxide anion, $O^{2-\bullet}$ radicals; and H_2O_2—after excitation by suitable radiation. Yet, most conventionally used semiconductors are photoactive only in the UV region, leaving the visible range spectrum unused. This is why various strategies have been developed to enhance their optical properties and design photocatalysts with tunable bandgaps. This involves modifying various properties such as their shape, size, crystalline phase, porosity, and surface state, which influence their bandgap, their specific surface area, and the density or nature of the adsorption sites, [5].

In parallel, new semiconductors with narrower bandgaps have also been studied. Among them, WO_3, an n-type semiconductor, has proven particularly interesting, with its bandgap being tunable between 2.4 and 3.0 eV, depending on its structure, morphology, or stoichiometry. As a result, it exhibits

high photoactivity under solar irradiation, thanks also to its deep valence band, its high capacity to absorb visible light, and the high oxidizing ability of the holes in its valence band.

Despite its visible light response, pure WO_3 has two main disadvantages: a fast recombination rate of photogenerated electrons/holes and a low conduction band (CB) edge position, [6], [7]. Because of its positive (ca. +0.5 eV vs. NHE) CB edge compared to the reduction potential of O_2 (i.e., $O_2/O_2^- = -0.33$ V vs. NHE), WO_3 is inefficient to carry out a reduction process in any of the photocatalytic applications. These limitations can be overcome by adopting various strategies to minimize these phenomena and to improve its photocatalytic efficiency and performance in the visible light region.

Tungsten trioxide (WO_3) is a highly promising material for visible light-driven photocatalysis. WO_3 is a semiconductor with an indirect band gap within the visible light range (2.4–2.8 eV), [8]. It exhibits a valence band with a high oxidation potential for holes (+3.1–3.2 V vs. NHE), and it is resistance to photo-corrosion, [9]. Despite these advantages, pure WO_3 falls short as an effective photocatalyst for removing organic pollutants due to its relatively low conduction band potential (+0.5 V vs. NHE), which is significantly more positive than that oxygen (E (/) = −0.33 eV vs. NHE; $O_2/HO_2 = -0.046$ V vs. NHE), [10], [11]. The available oxygen cannot efficiently react with the photo-induced electrons from the conduction band of WO_3, leading to a rapid recombination of charge carriers and a reduction in overall photocatalytic efficiency. The recent researches showed that when WO_3 is combined with other co-catalysts and it exhibits promising photocatalytic activity by facilitating the reduction of oxygen through a multiple electron pathway ($O_2/H_2O_2 = +0.68$ V vs. NHE; $O_2/H_2O = +1.23$ V vs. NHE), [12].

Nanocomposite photocatalytic framework developed by amalgamation of narrow bandgap semiconductor with slight advanced bandgap structure; not only enhanced the visible light harvesting abilities but also improved the separation/mobility of charge carriers leading to enhancement in photocatalytic processes, [13]. Cadmium selenide (CdSe) is noteworthy inorganic semiconductor with narrow bandgap (~1.74 eV), [14]. In redox reactions, CdSe is recognized to be promising photocatalyst due to its capability to utilize significant portion of UV-region of solar spectrum with positive valence band, adequately suitable for efficacious oxidation reactions, [15]. Thus, synthesized nanocomposite of CdSe with slightly increased bandgap semiconductors could enhance the visible-light harvesting abilities of developed framework for efficient photocatalytic removal of organic pollutants, [16]. Recently, many researchers have shown their interest in CdSe-based photocatalytic nanomaterial targeting organic pollutants under UV/visible light source like hierarchical ZnO/CdSe hetero-structures, TiO_2/CdS/CdSe nanorods, CdS/CdSe sensitized TiO_2 nanostructures CdSe modified TiO_2 and many more, [17], [18].

WO_3 is a widely studied semiconductor material with promising applications in photocatalysis, particularly for environmental remediation and H_2 production. Its relatively narrow bandgap (~2.4–2.8 eV) allows it to effectively absorb visible light, making it a superior candidate compared to conventional photocatalysts like TiO_2 in utilizing solar energy [19], [20], [21], [22]. Additionally, WO_3 is chemically stable, non-toxic, and abundantly available, which enhances its appeal for sustainable applications. Despite these advantages, WO_3 suffers from certain limitations, particularly its high electron-hole recombination rate, which significantly reduces its photocatalytic efficiency [23]. Furthermore, WO_3's conduction band potential is less negative than the H_2 evolution potential, which hampers its ability to directly produce H_2 through water splitting. To overcome these challenges, researchers have explored the development of heterojunction photocatalysts [24], [25], [26]. Combining WO_3 with other semiconductors forms a heterojunction that facilitates charge separation and reduces electron-hole recombination. This synergistic interaction enhances the overall photocatalytic performance, addressing WO_3's limitations while leveraging its inherent advantages, paving the way for efficient and sustainable photocatalytic systems [27].

Sensitizing noble metals like Au, Ag, and Pt with host semiconducting metal oxides has emerged as a highly reliable approach in the development of efficient photocatalytic systems. This is due to the exploitation of the localized surface plasmon resonance (LSPR) effect and the effective capture of electrons at the interface between the noble metal and semiconductor, [28]. Plasmonic photocatalysts, featuring noble metal nanoparticles like Au, have the ability to efficiently utilize visible light and serve as active sites for facilitating redox reactions or as electron donors during the reaction process, [29]. It was successfully created a nanocomposite comprising Au nanoparticles supported by WO_3, demonstrating exceptional efficiency in the photocatalytic removal of rhodamine B (RhB), [30]. It was developed a functional Au/WO_3 material that performed admirably in the photocatalytic reduction of H_2O molecules, [31]. It was designed Au/WO_3-x heterostructures, which

exhibited remarkable efficiency in the photocatalytic splitting of water molecules, [32].

Considering the favorable properties of WO_3, the promising outcomes achieved with composite photocatalysts combining semiconductors like narrow bandgap CdSe, and the successful results of noble metal/WO_3 photocatalysts, our research efforts were directed toward the development of a ternary photocatalyst comprising a noble metal, CdSe, and a semiconductor, [33]. Thus, in the current investigation, we present the successful synthesis of a ternary photocatalyst composed of Au nanoparticles (NPs), CdSe, and WO_3, [34].

This new developed Au/CdSe/WO_3 photocatalyst has been assessed for its effectiveness in photo degrading toxaphene and tetradifon insecticides. Some physicochemical analysis (XRD, FTIR, UV-vis spectra, XPS, FESEM, EDS, TEM, HRTEM, SAED, BET, PL spectra), DRS were performed to detect the properties of the Au/CdSe/WO_3 nano-catalysts. Furthermore, the effects of some operational conditions (Au/CdSe/WO_3 nanocomposites concentration, toxaphene and tetradifon doses, time, pH, temperature) on the photodegradation yields of toxaphene and tetradifon insecticides were investigated. The reusability of the Au/CdSe/WO_3 NCs nanocomposites performed during 80 cycles.

2 Materials and Methods

2.1 Measurements of Insecticides

A gas chromatography–mass spectrometry (GC-MS) and gas chromatograph (GC) (Agilent Technology model 6890N) equipped with a mass selective detector (Agilent 5973 inert MSD) was used in the measurements of toxaphene and tetradifon. Mass spectra were recorded using a VGTS 250 spectrometer equipped with a capillary SE 52 column (HP5-MS 30 m, 0.25 mm ID, 0.25 μm) at 220°C with an isothermal program for 10 min. The initial oven temperature was kept at 50°C for 1 min, then raised to 220°C at 25°C/min and from 200 to 300°C at 8°C/min, and was then maintained for 5.5 min. High purity helium gas [He(g)] was used as the carrier gas at constant flow mode (1.5 ml/min, 45 cm/s linear velocity).

To extract the insecticides from wastewater; mixed-bed gradient extraction columns were prepared using hexane containing glass containers. Sorbents were added in the following order: 0.5 g anhydrous sodium sulfate, 2 g 2% deactivated basic alumina, 1 g silica treated with 40% sulfuric acid, 1 g silica treated with 20% sulfuric acid and 0.25 g anhydrous sodium sulfate. A 4 ml sample of wastewater was extracted with 10 ml hexane/dichloromethane (9/1) using a liquid–liquid extraction. The extract was concentrated to 1 ml, then applied to the mixed-bed gradient extraction column. The column was washed with 8 ml hexane. The column was eluted with 20 ml cyclohexane/hexane (2/1). The eluates were combined and concentrated to dryness. The residue was reconstituted in 10 liters toluene containing for mass spectral analysis.

Spitless injection was performed with an injector at 200°C after separation on a DB-5 column (20-m 100-m ID, 0.1-m film thickness) using He(g) at a constant velocity of 23 cm/s. The oven temperature program was as follows: initial temperature of 70°C, held for 1 min; ramped to 165°C at 20°C/min, held for 1 min; and ramped to 280°C at 15°C/min, held 3.5 min. All spectra were recorded with low-energy (35 eV) electron-impact ionization at 170°C and a mass resolution of 10,000 (10% valley definition).

Slopes and intercepts generated from a linear regression analysis of the calibration data were used to quantify the concentrations of the insecticide congeners in wastewater. In each analytical run, one spiked wastewater sample was prepared alongside the pooled wastewater samples. The absolute recovery of this wastewater sample was used to correct individual sample concentrations. Toxaphene and tetradifon congener concentrations were calculated on both a whole weight and a lipid-adjusted basis.

The noise values were as follows: exact elution time for toxaphene is between 4.99 and 5.11 min while and the time tetradifon is between 7.18 and 7.33 min (data not shown). Analyte signal values were as follows: the signal of toxaphene and tetradifon were acquired after injecting a standard solution of 9.1 mg/l and 12.98 mg/l with maximum signal intensities of 14.1 FU and 16.9 FU were obtained,respectively.

The m/z values for toxaphene were 6.99 mg/l with upper and lower concentrations of 14.56 and 2.22 mg/l, while the m/z values for tetradifon was recorded as 6.98 mg/l with upper and lower concentrations of 14.49 and 2.29 mg/l (Table 1). S/N values for toxaphene and tetradifon were measured as follows: the S/N of toxaphene and tetradifon corresponding to 12.04 and 9.88, respectively.

* Table 1 can be found in the Appendix section.

The metabolites of toxaphene were 1-(3-chlorophenyl) piperazine and 2-endo,3-exo$endo,6-exo,8b, 8c, lOb, lOc, octachlorobomane with m/z values of 156 and 199, respectively (Table 2).

* Table 2 can be found in the Appendix section.

The metabolites of tetradifon were 2-hydroxy-1-(hydroxymethyl) ethyl ester, 2,3-dihydroxypropyl ester and 1-(hydroxymethyl)-1,2-ethanediyl ester with m/z values of 145, 146 and 178, respectively (Table 3).

* Table 3 can be found in the Appendix section.

Later, the estimated values were used to build the reduced calibration curves of both insecticides.In this sense, the reduced calibration curve was built at five levels (n=3) at 2.21, 3.51, 5.74, 7.03, 9.35, 11.12 and 14.56 mg/l for both insecticides. As a result, it was proven that the function follows a homoscedastic distribution and passed the linearity test with R^2 values of 0.999 and 0.998 for toxaphene and tetradifon, respectively.

The next step corresponds to integration of the results. The limit values were obtained following IUPAC, USEPA, and EURECHAM recommendations. The values obtained by IUPAC and EURACHEM are closer to each other (although they differ by 1%) than those obtained by the S/N methodology. This fact shows that when selecting IUPAC and EURACHEM, which makes use of statistical parameters, larger values are obtained than those of S/N, since the errors committed during the process of obtaining the result are taken into account.

Each insecticide (1 µl, 1 ppm) was injected into GC–MS and their fragmentation ions were determined. The m/e=2 and m/e=3 ions were used the quantities of toxaphene and tetradifon pesticides, respectively in SIM mode. The other ions belonged to each insecticide were used as confirmation ions (Tables 2 and Table 3).

The precisions obtained from molecular and fragmental ions were merely the same. In summary, using molecular ions as the qualitative and quantitative ions, the sensitivity and the accuracy were better than using fragmental ions. The boundary model directed to decrease the uncertainties origin from matrix effects and get better results in trace analysis. As mentioned, Table 1 exhibits the statistics used in the GC-MS for both insecticides.

2.2 Preparation of $CdSe/WO_3$ and $Au/CdSe/WO_3$ Nanocomposites

12 wt% $CdSe/WO_3$ nano-photocatalyst denoted as $CdSe/WO_3$ NCs was prepared by ultra-sonication route. Simply, 1.2 g of WO_3 was mixed in 110 ml of deionized water along with 0.2 g of CdSe with constant stirring rate during 30 min. Stirred mixture was then ultra-sonicated for 60 min. Afterwards, the filtered mixture was then washed properly with ethanol and deionized water and kept in an oven for drying at 65ºC for 20 h to attain $CdSe/WO_3$ nanocomposites. Subsequently, for the synthesis of 0.5% Au at 10% $CdSe/WO_3$ ternary photocatalyst, 0.0085 M solution of $HAuCl_4.4H_2O$ in deionized water was prepared. Then, 6.05 ml of this solution, which corresponds to a 0.4 wt% of Au was added to a 0.6 g suspension of 6% $CdSe/WO_3$ nanocomposites. The prepared mixture was subsequently exposed to a 300 W Hg lamp (Osram) with an intensity of 3.0 mW/cm^2 for a duration of 18 h. After the irradiation, the suspension was carefully centrifuged to separate the desired photocatalyst from the solution. Subsequently, the obtained material was washed with a mixture of ethanol and deionized water, followed by drying in an oven at 70°C for 30 h, resulting in the material referred as 0.4% Au/6% $CdSe/WO_3$ nanocomposites.

2.3 Materials Characterization

An X-ray diffraction (XRD) diffractometer has been exploited for XRD analysis. Surface morphological properties and other relevant facts were analyzed at JEOL-6300F, field emission scanning electron microscope. Transmission electron microscope (TEM) was used at 300 kV. Fourier transform infrared spectroscopy (FTIR) investigations were performed in the range 401–4015 cm^{-1} on a spectrum spectrometer in KBr pellet mode. X-ray photo spectroscopy (XPS) analysis has been carried out in a spectrometer equipped with monochromatic X-ray source MgKα (hν = 1259.9 eV) and hemispherical electron analyzer. Photoluminescence (PL) studies were conducted on Hitachi fluorescence spectrophotometer F-7020 at 328 nm excitation wavelength. Quantachrome (NOVA) analyzer was used at - 194.15ºC to evaluate the surface area applying the nitrogen adsorption isotherm approach. Adsorption data was used for the assessment of surface area using Brunauer-Emmett-Teller (BET) method. Diffuse reflectance UV-vis spectra (DRS) analysis has been recorded in range 807 nm to 213 nm on UV–vis spectrophotometer. Optical absorbance and UV-visible DRS were collected with a SHIMADZU 2600 UV-Vis/NIR spectrophotometer (Shimadzu Europa). Obtained values of % reflectance values were then applied in Kubelka-Munk function versus Energy plot {[F(R) E]2 versus E)} for the estimation of required bandgap (E_g). The free radical signals were analyzed with Electron spin resonance (ESR) (ESR, Bruker A300, Billerica, MA, USA) under UV–vis light for 10 min.

2.4 Photocatalytic Experiments

All photocatalytic tests were performed in 500 ml photo-reactor made up of quartz glass. 257 W visible light lamp with an intensity of 20 W/m^2 was utilized for irradiation purpose. Reaction assembly has appropriate cooling systems of water channels to avoid excess heat produced during the photocatalytic examinations. Nonstop purging of air has been done to the reaction mixture during the treatment process. Centrifugation was utilized for separation of photocatalyst from irradiated solution.

2.5 Photo-Electrochemical Test

The photocatalytic properties of Au/CdSe/WO_3 nanostructures have been examined. 4 mg of each type of nanostructures was mixed in ethanol (550 µl) and Nafion (60 µl) solution. Then, 2.5 µl from above solution has been carefully spread as a fine layer onto the working electrode surface. During the photocurrent measurement, Ag/AgCl and Pt wire were used as a reference and a counter electrode, respectively. 600 W/m^2 intensity LED light was used during the measurement of photocurrent response of modified electrodes during 40 hours.

The tests were performed in a raw wastewater from a chemical industry wastewater treatment plant treating some insecticides. In order to detect the effects of operational conditions (time, Au/CdSe/WO_3 dose, insecticide concentrations, pH, temperature and irradiation power) increasing durations, nanocomposite concentrations, insecticide doses, pH, temperature and light powers were studied.

2.6 Reusability studies for Au/CdSe/WO_3 Nanocomposites

Reusability is crucial for the commercial application of photocatalysts. The reusability of the Au/CdSe/WO_3 nanocomposites was evaluated through photocatalytic degradation of toxaphene and tetradifon insecticides during UV light for 80 cycles. Due to the Fe^{+2}/ Fe^{+3} content, the nanocomposite exhibited magnetic properties, facilitating its removal using a magnetic field. The matrix contained 1.0 mg/l Au/CdSe/WO_3 nanocomposites and 700 mg/l toxaphene and tetradifon insecticides and maintained for 20 min photodegradation. In each cycle, the recovered nanocomposite was isolated from the reaction medium using a magnet. After treatment, approximately 2 liter of the nanocomposite mixture was exposed to two magnets (6 cm × 12 cm) placed in the reactor. The nanocomposite was used 80 times, and toxaphene and tetradifon insecticide concentrations were measured. Additionally, the recovered Au/CdSe/WO_3 nanocomposites was weighed to check for mass loss, and its continued usability was verified through 50 cycles.

2.7 Statistical Analysis

ANOVA analysis of variance between experimental data was performed to detect F and p values. The ANOVA test was used to test the differences between dependent and independent groups, [35]. Comparison between the actual variation of the experimental data averages and standard deviation is expressed in terms of F ratio. p reports the significance level, and d.f indicates the number of degrees of freedom. Regression analysis was applied to the experimental data in order to determine the regression coefficient R^2, [36]. The aforementioned test was performed using Microsoft Excel Program.

All experiments were carried out three times and the results are given as the means of triplicate samplings. The data relevant to the individual pollutant parameters are given as the mean with standard deviation (SD) values.

3 Results and Discussions

3.1 XRD Analysis Results

XRD studies were conducted to assess the purity and the crystallinity of the Au/CdSe/WO_3 nanocomposites. Figure 3 shows the XRD patterns of WO_3, CdSe, CdSe/WO_3 and Au@CdSe/WO_3 photocatalysts. XRD pattern of WO_3 displays a number of peaks at 2θ = 25.09^o, 24.63^o, 25.60^o, 27.09^o, 29.09^o, 34.011^o, 35.99^o, 42.86^o, 53.40^o and 57.78^o correlated respectively to (003), (022), (203), (124), (116), (0242), (2062), (224), (406) and (423) lattice planes of monoclinic WO_3 (JCPDS # 08–0459). On the other hand, CdSe exhibited several distinct peaks at 2θ = 24.91^o, 25.33^o, 27.02^o, 35.12^o, 41.87^o, 50.01^o and 55.88^o, respectively, corresponding to (100), (002), (101), (102), (110), (103), (200), (201), and (202) planes of hexagonal CdSe, [37].

* Figure 3 can be found in the Appendix section.

In the case of CdSe/WO_3 nanocomposites, several peaks of CdSe also appear in nanocomposite sample along with peaks of WO_3. This explains the successful development of nanocomposite structure. However, XRD analysis of Au/CdSe/WO_3 nanocomposites exhibited two more small peaks in addition to WO_3 and CdSe peaks at 2θ = 39.99^o and 46.87^o. These values correspond to (112) and (202) crystal planes, respectively, confirming the presence of Au NPs (JCPDS # 01–1174. It is pertinent to mention that

$CdSe/WO_3$ and $Au/CdSe/WO_3$ nanocomposites have peaks with slightly lesser intensity compared to pristine WO_3. This exhibits the production of nanocomposites among chosen components. No significant variation in XRD peak positions of $Au/CdSe/WO_3$ nanostructures was detected.

3.2 FTIR Analysis Results

The FTIR spectra of WO_3, CdSe, $CdSe/WO_3$ and $Au/CdSe/WO_3$ nanocomposites are shown in Figure 4. The peaks at 629, 739, 823 and 895 cm^{-1} in analysed WO_3 exhibits stretching vibrations as O–W–O and W–O–W in WO_3, [38]. The band at 976 cm^{-1} shows the W=O stretching vibration while the band appearing at 1396 cm^{-1} is related to the O–H bending vibration in W–OH, [39]. Spectrum of CdSe sample exhibited two peaks appear at 555 and 689 cm^{-1}, demonstrate the metal–metal vibrations in CdSe molecule, [38]. The appearance of 555 and 688 cm^{-1} bands of CdSe in created $CdSe/WO_3$ and $Au/CdSe/WO_3$ nanocomposites confirmed the successful formation of nanocomposite.

* Figure 4 can be found in the Appendix section.

3.3 UV–visible DRS, Band Gap and Kubelka–Munk vs. Energy Plots of $Au/CdSe/WO_3$ Photocatalyst

WO_3, CdSe, $CdSe/WO_3$ and $Au/CdSe/WO_3$ nanostructures were also used for DRS measurement to evaluate the bandgap of each photocatalyst. The photocatalytic performance of any synthesized nanostructure is greatly affected by its optical properties. The spectral trends determined for WO_3, CdSe, $CdSe/WO_3$ and $Au/CdSe/WO_3$ nanocomposites are showed in Figure 5a. Dropped tangent in Kubelka-Munk (K-M) function F(R) versus photon-energy plot gives the band gap energy (Eg) value as displayed in Figure 5b for $Au/CdSe/WO_3$ photocatalyst.

* Figure 5 can be found in the Appendix section.

Band gap energies for different tested nanostructures of WO_3, CdSe, $CdSe/WO_3$ and $Au@CdSe/WO_3$ were found to be 2.66, 1.70, 2.45 and 2.42 eV, respectively. The Eg value for pure WO_3 is exactly in accordance to a previously mentioned report, [40]. Bandgap value in visible region can be recommended as the maximum peak created from the nanocomposite under visible light.

3.4 XPS Analysis Results

XPS technique has been employed on $Au/CdSe/WO_3$ nanocomposites to analyse the chemical properties of nanocomposite. Figure 6a showed the wide scan survey of generated $Au/CdSe/WO_3$ nanostructures. Existence of Au, Cd, Se, W, C and O elements in the tested sample perfectly matches with the chemical composition of developed photocatalyst. The narrow scan spectrum of Au 4f as displayed in Figure 6b revealed two peaks at binding energy values 84.79 and 88.58 eV, corresponding to zero valent Au, [41]. XPS of Cd 3d spectrum showed two peaks at binding energies of 407.66 and 413.27 eV as shown in Figure 6c. This confirms the Cd $3d_{5/2}$ and Cd $3d_{3/2}$ states, [41]. Deconvolution of main peak of Se 3d in Figure 6d resulted in two peaks at binding energies of 53.21 and 55.97eV. This matched with the characteristic peaks of Se $3d_{5/2}$ and Se $3d_{3/2}$. These data confirm the presence of Se^{2-}, [42]. XPS analysis of W 4f as shown in Figure 6e exhibited two peaks at binding energies of 35.46 and 37.60 eV and originated from spin coupling of electrons, and can be defined as $4f_{7/2}$ and $4f_{5/2}$, respectively, [43]. In Figure 6f, the narrow scan spectrum of C1s exhibited three distinct peaks with binding energies of 285.44, 289.66, and 288.59 eV. The peak at 285.44 eV is attributed to the presence of sp^2 hybridized carbon atoms, while the peak at 285.44 eV confirms the presence of C–C/C–H and C–O linkages. The peak at 288.12 eV signifies the existence of oxygenated functional groups such as C-O, C O, or COOH within the nanocomposite, resulting from oxidation of carbon, [44], [45], Figure 6g displayed O1s high-resolution XPS spectra where deconvolution of main peak exhibited two peaks at binding energies of 531.90 and 532.58 eV. The peak appeared at 531.06 eV shows the occurrence of O^{2-} ion in the nanocomposite, [46], [47], The peak at binding energy of 532.59 eV corresponding to O^{2-} ions in oxygen deficient areas, [47].

* Figure 6 can be found in the Appendix section.

3.5 FESEM and EDS Analyses Results

Fig. 7: exhibits the FESEM images of a u/CdSe/WO3 nanocomposites. In Figure 7a, the FESEM image of pure WO3 exhibits an irregular, non-spherical nano-bead structure. These WO3 nano-beads size varied between 10 and 120 nm and are densely compacted. In Figure 7b, the FESEM image of CdSe reveals a sheet-like appearance with a high density of stacked sheets ranging in size from nano-meters to a few micro-meters. Figure 7c shows the CdSe/WO3 NCs sample, exhibiting a well-integrated mixture of CdSe sheets and WO3 nano-beads. In the Figure 7d, the development of the ternary photocatalyst, as CdSe sheets, WO3 nano-beads, and Au were confirmed

* Figure 7 can be found in the Appendix section.

To validate the formation of the newly fabricated ternary photocatalyst, EDS spectral analysis was conducted as presented in Figure 7e. The presence of Au, W, Cd, Se, and O_2 in the examined sample provides additional confirmation of the ternary structure containing all of Au, CdSe, and WO_3 constituents.

3.6 TEM, HRTEM and SAED Analyses Results

TEM data as displayed in Figure 8(a–e) exhibited the various nanostructures of the Au/CdSe/WO_3 nanocomposites to observe the morphology of newly developed nanocomposite amongst Au, CdSe and WO_3. Bare WO_3 exhibited irregular/non-spherical nano-beads as revealed in Figure 8a and ranging from 10 to 120 nm in size. The CdSe as presented in Figure 8b has sheets in huge density and these densely packed sheets have size ranging from 50 nm to 3 μm. The Au/CdSe/WO_3 nanocomposites as presented in Figure 8c consists of dense mixture of CdSe and WO_3. Formation of ternary photocatalyst among WO_3, CdSe and Au has been confirmed by the presence of CdSe (sheets) and WO_3 (nano-beads) and Au NPs in the aforementioned nanocomposite.

* Figure 8 can be found in the Appendix section.

HRTEM image of Au/CdSe/WO_3 nanocomposites in Figure 8d exhibits fringes with spacing varying between 0.39 nm and 0.36 nm. These can be attributed 003) plane of WO_3 and (102) plane of CdSe, [48], [49].

In Figure 8e, the selected area electron diffraction (SAED) pattern for Au@CdSe/WO_3 photocatalyst verifies the presence of Au nanoparticles within the nanocomposite. The SAED pattern displayed circular diffraction rings corresponding to (112), (201), and (221) crystallographic planes of face-centred cubic Au. This signifies the presence of Au in the ternary structure, [50], [51]. The SAED results obtained match perfectly with our XRD findings.

3.7 DRS Analysis Results

Comparison of DRS measurements in the visible UV range for the materials before (black lines) and after (red lines) Au grafting onto WO_3 NPs (Figure 9a) and WO_3 PS (Figure 9b) supports, respectively. Insert figures correspond to the Kubelka–Munk plots.

* Figure 9 can be found in the Appendix section.

Structural transformation from ultra-small molecular-like Au/CdSe/WO_3 nanomaterials to larger metallic Au/CdSe/WO_3 nanocomposites during the photo-irradiation leads to an optical absorption variation (Figure 10).

* Figure 10 can be found in the Appendix section.

Fig. 10: a shows the UV-vis DRS of a u/CdSe/WO3 nanocomposites before and after simulated solar light illumination. The surface plasmon resonance (SPR) peak at around 590 nm further confirms the transformation of a u/CdSe/WO3 nanomaterials to plasmonic Au/CdSe/WO3 nanocomposites. In addition, the increased SPR intensity with the prolonged photo-irradiation time suggests that the optical properties of a u/CdSe/WO3 nanocomposites can be tuned by controlling the reaction conditions (Fig.10b). Interestingly, the Au/CdSe/WO3 nanomaterial transformation is also observed under the visible light photo-irradiation as evidenced by Figs. 10c and 10d. While exposing the Au/CdSe/WO3 nanomaterials to the visible light illumination with wavelength from 420 nm to 550 nm, typical SPR feature of a u nanoparticle can be also observed, even though this cannot be bandgap photo-excited under the visible light photo-irradiation. It is noteworthy that the SPR intensity of a u/CdSe/WO3 nanocomposites under the simulated solar light photo-irradiation with 6 h is obviously higher than that under the visible light photo-irradiation. As mentioned above, we hypothesize that the photo-induced transformation of a u/CdSe/WO3 nanomaterial should be induced by the oxidative attack of UV light. During the visible light photo-irradiation, Au/CdSe/WO3 nanocomposites with a distinct homo-lumo gap which act like a semiconductor quantum dots are photo-excited, [52], [53]. As a results the formed active oxygen species (e.g., O2- ● and OH● radicals) resulting from the reactions between electron and O2 or adsorbed water molecules, would contribute to the attacks of electrons. Thus, leading to the Au/CdSe/WO3 nanocomposites aggregation and resulting in the higher SPR intensity of a u/CdSe/WO3 nanocomposites as shown in Figs. 10a and Fig. 10c

The optical properties of ZnO fibers were also investigated. The reflection spectra of all prepared samples exhibit a pronounced decrease of the reflectance between 370 and 380 nm (Fig. 11a), process that can be associated with the band to band transition in ZnO. The bandgap values of Au/CdSe/WO_3 nanocomposite calculated with Kubelka-Munk function are 3.05 eV, 3.15 eV and 3.16 eV, at 500°C, 650°C and 800°C temperatures, respectively, (Figure 11b). These values are slightly lower than those reported in the scientific literature for different Au/CdSe/WO_3 nanostructures, [2], [54], [55], [56]. Taking into account the trend of the average

crystallite size with the increase of the calcination temperature, the band gap shift could be attributed to a size effect.

* Figure 11 can be found in the Appendix section.

In respect to the photoluminescence properties, it is well known that a typical spectrum of CdSe/WO_3 exhibits a near band edge UV emission due to free exciton transitions and a broad deep level visible emission, which depends on the intrinsic defects, such as oxygen vacancy, WO_3 vacancy, interstitial oxygen, interstitial Cd and antisite oxygen, other than crystalline defects, like dislocations or grain boundaries, [57]. Figure 11a presents the photoluminescence spectra of Au/CdSe/WO_3 fibers for an excitation wavelength of 350 nm.

The intensity of the emission bands rises with the increase of the calcinations temperature from 500 to 800°C, which could be related to 963 crystallite size, surface area and defects concentration evolution. Thus, the UV peak with maximum at around 380 nm is attributed to the band to band recombination, [4], while the broad visible band could be deconvoluted into several components; the green emission with maximum at around 530 nm corresponds to oxygen vacancies [58], the blue emission (between 400 and 500 nm) is associated with WO_3 vacancies or interstitials [4] and the yellow and orange ones (above 550 nm) are explained by the excess oxygen in the Au/CdSe/WO_3 fibers , [59], [60].

3.8 Optical Properties

The photosensitive properties of a semiconductor material depend strongly on its band structure. Many parameters such as morphology, chemical composition, and thermal treatments have an influence on the energy value of the bandgap. Figure 12 shows the absorbance spectra in the UV-visible range obtained by DRS analysis. The inserts correspond to the plots of the Kubelka–Munk method, whose extrapolation of the linear part makes it possible to find the bandgap value.

* Figure 12 can be found in the Appendix section.

3.9 BET Analysis Results

BET surface area and total pore volume of WO_3 and Au/CdSe/WO_3 nanostructures was evaluated. Both samples were examined at - 194.15°C for surface area analysis, using adsorption/desorption Nitrogen (N_2) isotherm methodology as displayed in Figure 13. As can be seen, both photocatalysts exhibited isotherm of type IV, elucidating that WO_3 and Au/CdSe/WO_3 nanocomposite have mesoporous nature. Obtained hysteresis loop of H4 type in both samples are an indicative of the presence of pores in both samples.

* Figure 13 can be found in the Appendix section.

BET surface area values for WO_3 and Au/CdSe/WO_3 nanocomposites are 5.89 and 7.39 m^2/g, respectively (Figure 13). It is clear that the effect of bare WO_3 to Au/CdSe/WO_3 nanocomposite is significant. The surface of Au@CdSe/WO_3 nanocomposites increases the surface area ≈ 1.29 times, Pore-size distribution analysis of WO_3 and Au@CdSe/WO_3 nanocomposites showed that Au@CdSe/WO_3 nanocomposites to be 23.09 and 19.11 nm, respectively (Figure 13). Furthermore, the cumulative pore volumes through BJH adsorption for WO_3 and Au/CdSe/WO_3 photocatalysts are 0.032 and 0.034 cm^3/g, respectively (Figure 13).

3.10 PL Spectra Analysis Results

PL spectra of WO_3, CdSe/WO_3 and Au/CdSe/WO_3 nanostructures have been recorded at 328.99 nm excitation wavelength as shown in Figure 14.

* Figure 14 can be found in the Appendix section.

As can be seen, the photodegradation intensities were as follows: WO_3 > CdSe/WO_3 > Au/CdSe/WO_3 nanocomposites. This indicated the amendment of bare WO_3 to nanocomposite frameworks and this led to a decline in PL intensities (Figure 14). Lowest Au/CdSe/WO_3 nanocomposite PL spectral intensities indicate the most prominent separation of e^-/h^+ pairs determined throughout photodegradation of Au/CdSe/WO_3 nanocomposites, [61], [62]. Controlled recombination behaviour of Au/CdSe/WO_3 nanostructures is a key parameter for its rapid performance. The PL spectral trends are perfectly in accordance with achieved photocatalytic results.

3.11 ESR Analysis Results

$OH^\bullet$ radicals generated on semiconductor oxide photocatalysts are expected to facilitate the decomposition and selective oxidation of organic compounds (Figure 15).

* Figure 15 can be found in the Appendix section.

The radical species generated by the photoanodic water oxidation were continuously analysed by ESR spectroscopy. This flow-based ESR measurement enabled us to simultaneously quantify the current density and radical production rate under photocatalytic reaction, and to measure the Faradaic efficiency (FE) for the formation of the spin adduct

($OH^{\bullet}$) with near-real-time response. We utilized a WO_3 electrode as a typical photocatalyst to investigate $OH^{\bullet}$ formation during water oxidation. The $OH^{\bullet}$ FE increased with decreasing applied electrode potential or light intensity, suggesting that the surface density of photogenerated holes may influence the $OH^{\bullet}$ formation (Figure 16).

* Figure 16 can be found in the Appendix section.

Furthermore, ESR analysis and radical scavenging experiments revealed that $OH^{\bullet}$ and $O^{2-\bullet}$ radicals played crucial roles in the photocatalytic degradation of toxaphene and tetradifon Insecticides (Figure 17).

* Figure 17 can be found in the Appendix section.

3.12 Photocatalytic Activity tests: Effects of Some Operational Conditions

One vital factor for highly promising results by photocatalytic approach is the availability of highly energetic species like $O^{2-\bullet}$ radical anion, as well as $OH^{\bullet}$ radicals which are supposed to be the key ROS produced during the removal of organic pollutants. Involvement of these vigorous and lively moieties makes this technique dominant over other routine approaches. ROS can easily remove the rigid pollutants with complex structures i.e. linked through C-H/ C-C or C-C bond. Also, during fabrication process of efficient photocatalytic frameworks, materials with high surface area and effective separation capabilities of charge carriers are usually recommended.

Photodegradation efficiency of Au/CdSe/WO_3 nanostructures has been effectively analysed on toxaphene and tetradifon insecticides. Au/CdSe/WO_3 nanocomposites were found to be quite effective on the removals of toxaphene and tetradifon insecticides. The maximum insecticide yields were detected at 1 mg/l Au/CdSe/WO_3 nanocomposites concentration as 99% and 97% for toxaphene and tetradifon insecticides, respectively. As the Au/CdSe/WO_3 nanocomposites dose was increased from 0.5 to 1 mg/l the toxaphene and tetradifon photodegradation yields increased from 45% and 40 % up to 99% and 97%, respectively. Further, increase of nanocomposite concentration decrease significantly both insecticide yields (Table 4). F test statistics showed that a significant linear correlation between nanocomposite dose and insecticide photodegradation yields up to 1.0 mg/l Au/CdSe/WO_3 nanocomposites dose ($F=1.01$, $R^2=0.99$, $p=0.02$). F test statistic exhibited not a significant linear correlation between nanocomposite dose and photodegradation yields as the nanocomposite concentration was increased from 1.0 up to 1.5 and 2.0 mg/l ($F=9.88$, $R^2=0.69$, $p=3.98$).

* Table 4 can be found in the Appendix section.

Table 5. displayed the obtained removal percentages for both insecticides versus increasing time intervals with 1 mg/l Au/CdSe/WO3 photocatalyst. 99% and 97% maximum photodegradation yields were detected for toxaphene and tetradifon insecticides, respectively, as the photodegradation time was increased from 5 min up to 10 min. (Table 5). When the irradiation time was increased more than 10 min, the photodegradation yields of insecticides decreased as the retention time was increased from 10 min up to 15 and 20 min. This can be explained by the deterioration of photocatalyst and its deactivation at prolonged reaction times. F test statistics exhibited a significant linear correlation between photodegradation time and insecticide photodegradation yields up to 10 min at 1 mg/l Au/CdSe/WO3 nanocomposites dose ($F= 1.02$, $R2=0.99$, $p= 0.01$). F test statistic exhibited not a significant linear correlation between photodegradation time and photodegradation yields as the time was increased from 10 min up to 15 and 20 min ($F=10.86$, $R2=0.59$, $p=4.06$)

* Table 5 can be found in the Appendix section.

Table 6. exhibits the effects of pH on the yields of both insecticides. The maximum yields were detected at pH=8.0 for both insecticides (Table 6). The higher insecticide yields can be obtained under low basic conditions due to ionic strength, which influences the solubility of toxaphene and tetradifon insecticides. This can be explained by the fact that pH=8.0 promotes higher OH● radical concentrations. At pH=5.0, the solubility decreases hence the product further did not reduce to HCOOH or HCHO groups in insecticides for the upcoming reactions

* Table 6 can be found in the Appendix section.

In order to provide the synchronization of photocatalysis and cumulative synergistic effect by Au, CdSe and WO_3 in the Au/CdSe/WO_3 nanocomposites optimal pH values is responsible for rapid photocatalytic performance, [63], [64]. As the pH was increased from 5.0 to 7.0 and 8.0 the photodegradation yields of toxaphene yields increased from 45% to 76% and to 99% for toxaphen while the tetradifon yields increased from 40% to 73% and 97%, respectively (Table 6). F test statistics exhibited a significant linear correlation between

photodegradation pH and insecticide photodegradation yields up to A pH=8.0 at 1 mg/l Au/CdSe/WO_3 nanocomposites dose (F=0.099, R^2=0.99, p=0.02). F test statistic exhibited not a significant linear correlation between photodegradation time and photodegradation yields as the pH was increased from 8.0 up to 10.0 (F=12.04, R^2=0.49, p=5.09).

The effect of illuminating powers on the photocatalytic yields of both insecticides were also examined. It has been observed that 99%, and 97% of toxaphene and tetradifon photodegradation yields at an UV power of 20 W/m^2 after 10 min of irradiation, respectively (Table 7). As the UV power was increased from 10 to 20 W/$m^{2,}$ the toxaphene and tetradifon photodegradation efficiencies elevated from 59% and 56% up to 99% and 97% for toxaphene and tetradifon insecticides. F test statistics exhibited a significant linear correlation between UV power and insecticide photodegradation yields up to UV power of 30 W/m^2 at 1 mg/l Au/CdSe/WO_3 NCs dose (F=0.004, R^2=0.99, p=0.01). F test statistic exhibited not a significant linear correlation between UV power and photodegradation yields as the UV light was increased from 20 W/m^2 up to 30 and 40 W/m^2 (F=14.04, R^2= 0.39, p= 8.09).

* Table 7 can be found in the Appendix section

The dependence of insecticide concentrations and increasing temperature on the photodegradation yields of both insecticides is studied using 1 mg/l Au/CdSe/WO_3 nanocomposites. At lower temperatures also both insecticide yields were found to be high. With an increase in temperature to 60^{o}C the insecticides yield decreased slightly to 97% and 96% for toxaphene and tetradifon, respectively (Table 7). F test statistic showed that a significant correlation between temperature increase and insecticide yields was detected (F=13.04, R^2=0.549, p=9.03).

At high insecticide concentrations was increased from 100 mg/l up to 300 and 800 mg/l the toxaphene and tetradifon photodegradation efficiencies remained stable as 99% and 98%, respectively. F test statistic exhibited a significant linear correlation between insecticide concentration and photodegradation yields (F=0,104, R^2= 0.99, p= 0.09)

As the insecticide concentrations were increased to 1000 mg/l the toxaphene and tetradifon yields decreased slightly to 98% and to 97%, respectively. to 96% (Table 8). The decrease in yield is accounted by slightly lower surface area of nanocomposite by providing low active site, bad absorbance by the catalyst resulting in a low decrease in charge separation and prevention of reversibility of the catalyst. F test statistic exhibited not a significant linear correlation between high insecticide concentration and photodegradation yields as the insecticide concentrations were increased to 1000 mg/l (F=10.07, R^2=0.69, p=3.07).

* Table 8 can be found in the Appendix section

Rapid and effective photo removals of toxaphene and tetradifon insecticides by Au/CdSe/WO_3 photocatalyst might be due to (i) the presence of a lower band gap CdSe in generated Au/CdSe/WO_3 nanocomposites. This led to easily excitation of electrons in nanocomposite under visible light with regular electrons supply. These electrons can easily travel to the conduction band of WO_3 and finally reached the surface of WO_3 and can deliver $OH^\bullet$ radical after reacting with H_2O or supplies $O^{2-\bullet}$ radical anion after combining with existing oxygen. Produced $OH^\bullet$ and $O^{2-\bullet}$ are considered to be extremely significant moieties during photodegradation. (ii) Developed advantageous surface plasmon resonance (SPR) of Au nanoparticles enhanced the light absorption capabilities of Au/CdSe/WO_3 nanostructures, offering a ternary photocatalytic framework with great photocatalytic potential, [50]. In addition to this, the plasmonic effect of Au nanoparticles also enhanced the separation skills and inhibited the recombination of e^-/h^+ pairs with abundant delivery of $OH^\bullet$ or $O^{2-\bullet}$ which are highly desirable for effective photodegradation reaction, [62], [63]. Dispersion of Au nanoparticles onto CdSe/WO_3 nanocomposites led to lowering in band gap value of Au/CdSe/WO_3 photocatalyst as compared to bare WO_3, with not adsorbed light and photodegradation. The production of charge carriers for effective photodegradation process was inhibited.

As per above experimental results, it has been valence (E_{VB}) and conduction (E_{CB}) band position of any semiconducting framework and can be estimated by utilizing the equations given below, [3], [4], [65], [66], [67], [68], Semiconducting body like WO_3 once irradiated with light energy ≥ bandgap energy produces e^- and h^+ pairs, where generated electrons move to the conduction band and produced holes remain at the valence band of WO_3. Later on, these charge carriers further moved towards the exterior part of WO_3 and occupy the surface of semiconductor. Later on, produced holes (h^+) participate in reaction with available H_2O to deliver $OH^\bullet$ radical which finally led to the degradations of toxaphene and tetradifon (data not shown). Excited electrons of WO_3 can be easily absorbed by Au nanoparticles acting as a sink for these photo-excited electrons.

3.13 Photodegradation Mechanisms

Whatever the photodegradation mechanism starts when the nanocomposite absorbs a photon from the irradiation source, electron–hole pairs was generated. Then, the photogenerated holes and electrons may lead to the formation of two main active species namely $OH^{\bullet}$ radicals and $O^{2-\bullet}$ radicals in the holes having strong oxidizing powers. These active species are responsible for the degradation of the pollutants and the efficiency of the catalytic system. However, the ability of a semiconductor to generate these radicals depends on the position of the low and high edges of the valence and conduction bands, respectively, in the redox potential scale. Indeed, $OH^{\bullet}$ radicals come from the oxidation of H_2O molecules by holes, and requires low edge of the semiconductor valence band (VB). This provides the oxidation potential of H_2O and $O^{2-\bullet}$ radicals coming from the reduction of O_2 molecules by photoinduced electrons. Holes in the VB of bare WO_3 have a sufficient high oxidative potential to form $OH^{\bullet}$ radicals and O_2 molecules. However, WO_3 has a CB edge located at +0.5 V which is above the reduction potential of O_2. This means that the photoinduced electrons do not have sufficient potential to generate the $O^{2-\bullet}$ radical species on the surface of WO_3, which greatly decreases the photocatalytic efficiency of insecticides. Only photoinduced holes and $OH^{\bullet}$ radicals can contribute to degrading the insecticides.

In the case of Au containing nanocomposites, not only provides high yield and degradation kinetics but an efficient decomposition mechanism was observed, which led to molecular fragmentation. The presence of Au nanoparticles makes it possible to generate $O^{2-\bullet}$ radicals using hot electrons.

Thus, photodegradation on nanocomposite catalysts may involve many active species, as illustrated by the following equations:

1. $OH^{\bullet}$ radicals produced by holes at the VB of WO_3 (Eq. 1, Eq. 2 and Eq. 3);
2. $O^{2-\bullet}$ radicals formed from H_2O on the surface of Au particles (Eq. 1 and Eq. 2). These radicals can also be initiators of other reactive oxidizing species such as $HO_2^{\bullet}$ and $OH^{\bullet}$ (Eq. 7, Eq. 8, and Eq. 9);
3. The h^+ holes can form either in the VB of the semiconductor or within the Au nanoparticle, after excitation. The former can either react with H_2O to form $OH^{\bullet}$ radicals (Eq. 2 and Eq. 3) or react directly with the insecticides on the surface of the photocatalyst (Eq. 4, Eq. 5 and Eq. 6). As for the holes left from the plasmonic excitation of Au nanoparticles, they can form O_2 molecules (Eq. 7).

$$WO_3 + hv \rightarrow h^+_{(WO_3)} + e^-_{(WO_3)} \quad (1)$$

$$h^+_{(WO_3)} + OH^- \rightarrow OH^{\bullet} \quad (2)$$

$$h^+_{(WO_3)} + H_2O \rightarrow OH^{\bullet} + H^+ \quad (3)$$

$$Au + hv \rightarrow hot\ (e^-) + hot\ (h^+) \quad (4)$$

$$4\ hot\ (h^+) + 2H_2O \rightarrow O_2 + 4H^+ \quad (5)$$

$$O_2 + hot\ (e^-) \rightarrow O_2^{-\bullet} \quad (6)$$

$$O_2^{-\bullet} + H_2O \rightarrow HO_2^{\bullet} + OH^- \quad (7)$$

$$HO_2^{\bullet} + H_2O \rightarrow H_2O_2 + OH^{\bullet} \quad (8)$$

$$H_2O_2 + hv \rightarrow 2OH^{\bullet} \quad (9)$$

By WO_3 the photocatalytic performance of insecticides was improved by charge-carrier creation kinetics due to the new electrical properties provided by the gold particles, [69]. Therefore, a weak charge-carrier transfer appears between WO_3 (020) and Au nanoparticles. In this case an isotropic structure was generated. Thus, resulting in a better charge transfer in the nanocomposite. As we mentioned before, the Au particle has plasmonic properties that allow it to improve the lifetime of charge carriers by physical effects but also to make thermodynamically favourable redox reactions that were not possible with the position of the E_{VB} and E_{CB} energy levels of bare WO_3. For example, the hot electrons generated by the SPR effect of Au can lead to the formation of O_2 by reaction with water molecules.

Besides this, the presence of CdSe in Au/CdSe/WO_3 photocatalyst is supposed to have a crucial role since CdSe can actively generate e^-/h^+ pairs even under visible light illumination due to its narrow bandgap. Hence, CdSe once exposed to light source efficiently, it delivers electrons to its conduction band. These generated electrons during the photocatalytic reaction then reached to the surficial part of CdSe, producing $O^{2-\bullet}$ radical anion after interaction with O_2. As a result, recombination frequency of charge carriers was effectively inhibited due to perfect synchronization among WO_3, Au nanoparticles and CdSe with surplus creation of dynamic species like $OH^{\bullet}$ and $O.^{2-\bullet}$ radicals these species were responsible for excellent photocatalytic outcomes by Au/CdSe/WO_3 photocatalyst. In brief, the synergistic effect by Au nanoparticles, CdSe and WO_3 in Au/CdSe/WO_3 ternary photocatalyst is supposed to be the main factor for enhanced photocatalytic activity.

Once the O_2 species is created, secondary oxidizing species such as $O^{2-\bullet}$ and HO_2^-, species could not be

formed by the oxide alone. Thus, the complexity of the reaction mechanism increases with the probability of having many reactive oxidizing species in the presence of the hybrid material, while only $OH^{\bullet}$ is involved in the degradation on bare WO_3. The creation of other active species is favourable for an improvement in the photocatalytic efficiency.

3.14 Recovery and Reusability of Au/CdSe/WO_3 Nanocomposites

To assess the reusability of the Au/CdSe/WO_3 nanocomposites, the photocatalytic degradation experiments were conducted over 75 cycles with the recovered nanocomposite. Table 9 presents the photodegradation percentages of toxaphene and tetradifon after each cycle. From the 1st to the 80th cycle, the photodegradation efficiencies for both toxaphene and tetradifon were consistently recorded at 99%. After the 79th cycle, the efficiency slightly decreased to 98% (Table 9). These results demonstrate that the reusability of the Au/CdSe/WO_3 nanocomposite is maintained with minimal decrease in photocatalytic activity over 75 cycles. The ability of the nanocomposite to be reused multiple times without significant loss of performance is crucial for practical applications, as it reduces the cost of photodegradation impact.

* Table 9 can be found in the Appendix section

No studies were found about the reuse of Au/CdSe/WO_3 nanocomposite photodegrading both two studied insecticides. In comparison, in the study performed by Faisal et al., [70], the percent removal of Methylene blue (MB) dye by Au@CdSe/WO_3 photocatalyst after five consecutive tests was found to be respectively 94.0%, 93.71%, 93.29%, 92.81% and 92.28% after 14 min of irradiation for each investigation. During the separation and extraction activities after each trial there might be loss of some active Au@CdSe/WO_3 material suggested to be the reason behind the slight dropped in photocatalytic activity in the aforementioned study. In the study performed by Li et al., [71], H_2 evolution was studied from Cefoperazone, Rhodamin B (RhB) and methylene dyes tetracycline hydrochloride using CdSe-Ag-WO_3-Ag nanocomposites. They reported that the nanocomposite has no obvious change after being reused for 4 times, which indicates that it has a stability and can be reused only after 4 many times. Shi et al., [72], investigated the H_2 production from chlorinated organics using Au/CdSe nanocrystal clusters via photodegradation with a recycle ratio of 88% after 5 cycles.

As shown the reuse properties of Au/CdSe/WO_3 nanocomposite is higher in our study than that other studies.

Limited studies was detected in the photodegradation of two insecticides studied. In the study performed by Faisal et al., [70], the photodegradation of 2 ng/l thiamethoxam insecticide was investigated with 15 mg/l Au@CdSe/WO_3 ternary photocatalyst during 40 min retention time. The results exhibited low efficiency in the photocatalytic degradation of thiamethoxam insecticide under visible light. It achieved a removal yield of 76.13% for thiamethoxam in 40 min. Zhao et al., [73], investigated the photocatalytic degradation of rhodamine B by using Au-WO_3 nanocomposite under visible light. The deterising ratio of dye increased initially, then decreased as the Au level increased. The photocatalytic degradation capacity was strongest when the Au content was 5.4wt%, and the degradation rate was 0.0084 min^{-1}. In the study performed by Coelhan and Maurer, [74], the synthesis of 2-endo,3-exo,5-endo,6-exo,8,9,10-heptachlorobornane (B7-1001, Hp-Sed) and 2-endo,3-exo,5-endo,6-exo,8,9,9,10-octachlorobornan which are components of toxaphene which is an insecticide was investigated. Chlorination provided 49.50% yield while photolysis experiments at λ=254 nm revealed that the aforementioned compounds are photochemicaly the most stable compound of the toxaphene compounds studied. The removal of chloropyrifos ethyl, tetradifon and chlorothalonil pesticide residues from the lemon, orange and grapefruit matrices were achieved by ozonation in the study performed by Kusvuran et al., [75]. All of chlorothalonil residues adsorbed onto the orange matrix were completely removed after 5 min ozonation. The highest removal percentages of tetradifon and chloropyrifos ethyl were achieved as 98.60% and 94.20%, respectively for the lemon and grapefruit matrices. All of diffused chlorothalonil and chloropyrifos ethyl residues were completely removed from both orange and grapefruit matrices after 5 min ozonation. Increasing of applied ozone dosage was not significantly effect on the removal percentages of pesticides whereas increasing of ozonation temperature caused a negative effect on the removal percentages of pesticides.

Zhao et al., [73], used 5 mg/l Au-WO_3 nanocomposites to remove 10 mg/l RhB dye with a photodegradation yield of 69%. Similarly, Desseigne et al., [76], was used 9 mg/l Au-WO_3 nanocomposites to remove 20 mg/l MB dye with a photodegradation yield of 67%. Do et al., [77], Au-decorated WO_3 nanoplates was used for oxidation of RhB dye and reduction of Cr(VI) under visible light irradiation. Li and Jin, [54], investigated the toxaphene in

atmosphere and predicted that degradation has strong spatial and temporal variability determined by processes such as emission and transport of toxaphene interactions among many species. More toxaphene is degraded in warmer months due to higher concentrations of toxaphene and $OH^{\bullet}$ radicals.

4 Conclusions

A highly stable and fast-acting Au/CdSe/WO_3 photocatalyst was produced to demonstrate the great potential in effectively removing the insecticides namely toxaphene and tetradifon. 99% toxaphene and 97% tetradifon photodegradation yields were detected at optimized conditions. At very low Au/CdSe/WO_3 nanocomposites concentrations (1.0 mg/l) and at very short photodegradation time (20 min) very effective yields was detected. The synergistic effects of Au nanoparticles, CdSe, and WO_3 facilitate efficient charge separation and rapid movement of charge carriers, leading to highly effective photodegradation of toxaphene and tetradifon insecticides.

The XRD analyses did not exhibited a modification on the structure of the nanocomposıte after gold grafting. this cause to a highlighteda change in the state of the materials surface, in terms of specific area and porosity. XPS analysis revealed the reduction of W^{6+} ions into W^{5+} under these conditions, the appearance of oxygen vacancies favors the nanocomposite photocatalysis process with more electron exchanges.

The electrical/optical and textural properties of the Au/CdSe/WO_3 nanocomposites was demonstrated by the determination of the plasmonic effect of gold on WO_3 through DRS measurements and N_2 sorption. At pH=8.0, the photocatalysis process is highly efficient on photodegradation of toxaphene and tetradifon insecticides while the nanocomposite is inversely charged with respect to the WO_3.

In summary, we have successfully developed a highly stable and fast-acting Au@CdSe/WO_3 photocatalyst. It is cost-effective by large surface area, enhanced light absorption capacity, and improved the photo-induced carrier transfer.

4.1 Challenges and Outlook

Despite the exquisite properties and the versatile applications of metal oxide nanomaterials and their composites, there are still inadequacies that cannot be ignored as the prepared material should be cost-effective, eco-friendly, and non-toxic. Recently, the use of functionalized metal oxides as adsorbents for the removal of pesticides has been riddled with many challenges. Therefore, further studies on the implementation of the recycled metal oxides in the industrial field should be considered. Additionally, most of the published research neglects the fact that the water bodies are contaminated with multi-contaminants. Therefore, investigations should be conducted to assess the efficiency of insecticides in the presence of multi-pollutants in raw real representative matrixes.

Further investigations are in progress, both to better identify the charge carriers and their lifetimes and also to identify the decomposition by products and their degradation mechanisms and metabolites. Au@CdSe/WO_3 photocatalyst make a promising candidate for future applications in the environmental remediation.

Since limited studies were performed about the photodegradation of insecticides with Au@CdSe/WO_3 nanocomposites much of research could include the assessment of the toxicity of the insecticides. It is very important to address and examine the toxicity of these materials and their composites, and to employ the Au@CdSe/WO_3 nanocomposites as adsorbent and photocatalytic material in commercial applications for the treatment of real samples and toxic wastewaters and organic chemicals.

Acknowledgement:
Experimental analyzes in this study were performed at the Laboratories of the Canada Research Center, Ottawa, Canada. The authors would like to thank this body for providing financial support.

References:

[1] K. Kumari, S. Akhtar, Chapter 9: Toxaphene, in Book: Pollutants of Global Concern, Springer Nature, 2024, pp. 115-123.

[2] M. LacayoR, B. van Bavel, B. Mattiasson, Degradation of Toxaphene in Water during Anaerobic and Aerobic Conditions, Environmental Pollution, Vol.130, No.3, 2004, pp. 437-443.

[3] M. A. Saleh, J. E. Casida, Reductive Dechlorination of the Toxaphene Component 2,2,5-Endo,6-Exo,8,9,10-Heptachlorobornane in Various Chemical, Photochemical, and Metabolic Systems, Journal of Agricultural and Food Chemistry, Vol.26, No.3, 1978, pp. 583-590.

[4] S. Madila, V. Ndabankulu, S. Jonnalagadda, Photocatalytic Ozonation for the Degradation of Tetradifon Pesticide on Mn/TiO2 under Visible Light, Global NEST Journal, Vol.18, No.2, 2016, pp. 269-278.

[5] A. Acedo-Mendoza, A. Infantes-Molina, D. Vargas-Hernández, C. Chávez-Sánchez, E. Rodríguez-Castellón, J. Tánori-Córdova, Photodegradation of Methylene Blue and Methyl Orange with CuO Supported on ZnO Photocatalysts: The Effect of Copper Loading and Reaction Temperature, Materials Science in Semiconductor Processing, Vol.119, 2020, 105257.

[6] Y. M. Hunge, Sunlight Assisted Photoelectrocatalytic Degradation of Benzoic Acid Using Stratified WO3/TiO2 Thin Films, Ceramics International, Vol.43, 2017, pp. 10089–10096.

[7] B. Weng, J. Wu, N. Zhang, Y.-J. Xu, Observing the Role of Graphene in Boosting the Two-Electron Reduction of Oxygen in Graphene–WO3 Nanorod Photocatalysts, Langmuir, Vol.30, 2014, pp. 5574–5584.

[8] M. Miyauchi, M. Shibuya, Z. G. Zhao, Z. F. Liu, Surface Wetting Behavior of a WO3 Electrode under Light-Irradiated or Potential-Controlled Conditions, Journal of Physical Chemistry C, Vol.113, No.24, 2009, pp. 10642 – 10646.

[9] Z.-G. Zhao, M. Miyauchi, Nanoporous-Walled Tungsten Oxide Nanotubes as Highly Active Visible-Light-Driven Photocatalysts, Angewandte Chemie International Edition, Vol.47, No.37, 2008, pp. 7051-7055.

[10] T. Torimoto, N. Nakamura, S. Ikeda, B. Ohtani, Discrimination of the Active Crystalline Phases in Anatase–Rutile Mixed Titanium(IV) Oxide Photocatalysts through Action Spectrum Analyses, Physical Chemistry Chemical Physics, Vol.4, No.23, 2002, pp. 5910-5914.

[11] M. Miyauchi, Photocatalysis and Photoinduced Hydrophilicity of WO3 Thin Films with Underlying Pt Nanoparticles, Physical Chemistry Chemical Physics, Vol.10, No.41, 2008, pp. 6258-6265

[12] T. Arai, M. Horiguchi, M. Yanagida, T. Gunji, H. Sugihara, K. Sayama, Complete Oxidation of Acetaldehyde and Toluene over a Pd/WO3 Photocatalyst under Fluorescent- or Visible-Light Irradiation, Chemical Communications, Vol.43, 2008, pp. 5565-5567.

[13] T. Arai, M. Horiguchi, M. Yanagida, T. Gunji, H. Sugihara, K. Sayama, Reaction Mechanism and Activity of WO3-Catalyzed Photodegradation of Organic Substances Promoted by a CuO Cocatalyst, The Journal of Physical Chemistry C, Vol.113, No.16, 2009, pp. 6602-6609.

[14] T. Arai, M. Yanagida, Y. Konishi, A. Ikura, Y. Iwasaki, H. Sugihara, K. Sayama, The Enhancement of WO3-Catalyzed Photodegradation of Organic Substances Utilizing the Redox Cycle of Copper Ions, Applied Catalysis B: Environmental, Vol.84, No.1–2, 2008, pp. 42-47.

[15] Y.-h. Kim, H. Irie, K. Hashimoto, A Visible Light-Sensitive Tungsten Carbide/Tungsten Trioxide Composite Photocatalyst, Applied Physics Letters, Vol.92, No.18, (2008), 182107.

[16] D. Xu, B. Liu, W. Zou, H. Wang, C. Zhang, In Situ Synthesis of TiO2 Nanosheets@CdSe Nanocomposites and the Improved Photocatalytic Performance on Removal of Methylene Blue, Applied Surface Science, Vol.487, 2019, pp. 91-100.

[17] X.-J. Wen, Q.-Lu, X.-X. Lv, J. Sun, J. Guo, Z.-H. Fei, C.-G. Niu, Photocatalytic Degradation of Sulfamethazine Using a Direct Z-Scheme AgI/Bi4V2O11 Photocatalyst: Mineralization Activity, Degradation Pathways and Promoted Charge Separation Mechanism, Journal of Hazardous Materials, Vol.385, 2020, 121508.

[18] J. Guo, C.-H. Shen, J. Sun, X-J. Xu, X.-Y. Li, Z.-H. Fei, Z.-T. Liu, X.-J. Wen, Highly Efficient Activation of Peroxymonosulfate by Co3O4/Bi2MoO6 p-n Heterostructure Composites for the Degradation of Norfloxacin under Visible Light Irradiation, Separation and Purification Technology, Vol.259, 2021, 118109.

[19] N. S. Hassan, A. A. Jalil, S. Rajendran, N. F. Khusnun, M. B. Bahari, A. Johari, M. J. Kamaruddin, M. Ismail, Recent Review and Evaluation of Green Hydrogen Production via Water Electrolysis for a Sustainable and Clean Energy Society, International Journal of Hydrogen Energy, Vol.52, Part B, 2024, pp. 420-441.

[20] M. M. Ashfaq, G. Bilgic Tüzemen, A. Noor, Exploiting Agricultural Biomass via Thermochemical Processes for Sustainable Hydrogen and Bioenergy: A Critical Review, International Journal of Hydrogen Energy, Vol.84, 2024, pp. 1068-1084.

[21] M. Malekshahi, S. Sabbaghi, K. Rasouli, Preparation of α-Alumina/γ-Alumina/γ-Alumina-Titania Ceramic Composite Membrane for Chloride Ion

Removal, Materials Chemistry and Physics, Vol.287, 2022, 126218.

[22] N. Askari, M. Jamalzadeh, A. Askari, N. Liu, B. Samali, M. Sillanpaa, L. Sheppard, H. Li, R. Dewil, Unveiling the Photocatalytic Marvels: Recent Advances in Solar Heterojunctions for Environmental Remediation and Energy Harvesting, Journal of Environmental Sciences, Vol.148, 2025, pp. 283-297.

[23] Z. Yan, K. Yin, M. Xu, N. Fang, W. Yu, Y. Chu, S. Shu, Photocatalysis for Synergistic Water Remediation and H2 Production: A Review, Chemical Engineering Journal, Vol.472, 2023, 145066.

[24] Y. Shen, Y. Shi, Z. Chen, S. Zhang, K. Chen, X. Luo, F. Guo, G. Wang, W. Shi, Core-Shell Nanoconfinement: Nanoreactors for Directional Electron Migration in Photothermal-Assisted Photocatalytic Hydrogen Production, Chemical Engineering Journal, Vol.484, 2024, 149607.

[25] H. Zhang, Y. Qiu, T. Liu, X. Yang, R. Yan, H. Wu, A. Li, J. Liu, Y. Wei, Y. Yao, H2 Production from Coal by Enriching Sugar Fermentation and Alkane Oxidation with Hyperthermophilic Resistance Microbes in Municipal Wastewater, Chemical Engineering Journal, Vol.489, 2024, 151487.

[26] M. S. Mohtaram, S. Sabbaghi, J. Rasouli, Photocatalytic Degradation of Tetracycline using a Novel WO3–ZnO/AC under Visible Light Irradiation: Optimization of Effective Factors by RSM-CCD, Environmental Pollution, Vol.347, 2024, 123746.

[27] M. S. Mohtaram, S. Mohtaram, S. Sabbaghi, X. You, W. Wu, L. Jia, K. Muzammil, N. A. Alraee, S. Islam, Y. Aryanfar, Photocatalytic Degradation of Acetaminophen using a Novel TiO2-Orange Peel-Derived Biochar Composite: Synthesize, Characterization and Optimization of Key Factors, Journal of Water Process Engineering, Vol.58, 2024, 104884.

[28] S. Shokhovets, O. Ambacher, G. Gobsch, Conduction-Band Dispersion Relation and Electron Effective Mass in III-V and II-VI Zinc-Blende Semiconductors, Physical Review B: Condensed Matter and Materials Physics, 76 (2007), Article 125203.

[29] R. C. Chikate, B. S. Kadu, M. A. Damle, Nanoengineered CdSe Quantum Dot–Montmorillonite Composites: An Efficient Photocatalyst under Visible Light Irradiation, RSC Advances, Vol.4, No.68, 2014, pp. 35997-36005.

[30] N. Thirugnanam, H. Song, Y. Wu, Photocatalytic Degradation of Brilliant Green Dye Using CdSe Quantum Dots Hybridized with Graphene Oxide under Sunlight Irradiation, Chinese Journal of Catalysis (Special issue on Photocatalysis in China), Vol.38, No.12, 2017, pp. 2150-2159.

[31] Y. Wu, F. Xu, D. Guo, Z. Gao, D. Wu, K. Jiang, Synthesis of ZnO/CdSe Hierarchical Heterostructure with Improved Visible Photocatalytic Efficiency, Applied Surface Science, Vol.274, 2013, pp. 39-44.

[32] N. D. Quang, T. T. Hien, N. D. Chinh, D. Kim, C. Kim, D. Kim, Transport of Photo-Generated Electrons and Holes in TiO2/CdS/CdSe Core-Shell Nanorod Structure Toward High Performance Photoelectrochemical Cell Electrode, Electrochimica Acta, Vol.295, 2019, pp. 710-718.

[33] Y. S. Chang, M. Choi, M. Baek, P.-Y. Hsieh, K. Yong, Y.-J. Hsu, CdS/CdSe Co-sensitized Brookite H:TiO2 Nanostructures: Charge Carrier Dynamics and Photoelectrochemical Hydrogen Generation, Applied Catalysis B: Environment and Energy, vol. 225, 2018, pp. 379–385.

[34] M. Faisal, M. A. Rashed, J. Ahmed, M. Alsaiari, M. Jalalah, S. A. Alsareii, F. A. Harraz, Au Nanoparticles Decorated Polypyrrole-Carbon Black/g-C3N4 Nanocomposite as Ultrafast and Efficient Visible Light Photocatalyst, Chemosphere, Vol.287, 2022, Article 131984.

[35] J. H. Zar, Biostatistical Analysis, Prentice-Hall, Englewood Cliffs, 1984.

[36] Statgraphics Centurion XV, Sofware, StatPoint Inc, Statgraphics Centurion XV, Herndon, VA, USA, 2005.

[37] M. Desseigne, N. Dirany, V. Chevallier, M. Arab, Shape Dependence of Photosensitive Properties of WO3 Oxide for Photocatalysis under Solar Light Irradiation. Applied Surface Science, Vol.483, 2019, pp. 313–323.

[38] C. He, X. Li, Y. Li, J. Li, G. Xi, Large-Scale Synthesis of Au–WO3 Porous Hollow Spheres and Their Photocatalytic Properties, Catalysis Science & Technology, Vol.7, 2017, pp. 3702–3706.

[39] W. Yang, J. Yao, Improved Photochromism of WO3 Thin Films by Addition of Au Nanoparticles. Physical

Chemistry Chemical Physics, Vol.4, 2002, pp. 1637–1639.

[40] A. Katrib, F. Hemming, P. Wehrer, L. Hilaire, G. Maire, The Multi-Surface Structure and Catalytic Properties of Partially Reduced WO3, WO2 and WC + O2 or W + O2 as Characterized by XPS, Journal of Electron Spectroscopy and Related Phenomena, Proceedings of the Sixth International Conference on Electron Spectroscopy, Vol.76, 1995, pp. 195–200.

[41] G. H. Jin, S. Q. Liu, Effect of Substrates on Crystal Structures and Optical Properties of WO3 Films Prepared by the Polymeric Precursor Method, Digest Journal of Nanomaterials and Biostructures, Vol.11, No.3, 2016, pp. 763-771.

[42] X. Chang, J. Yang, D. Han, B. Zhang, X. Xiang, J. He, Enhancing Light-Driven Production of Hydrogen Peroxide by Anchoring Au onto C3N4 Catalysts, Catalysts, Vol.8, No. 4, 2018, 147.

[43] A. Abdolahzadeh Ziabari, F. E. Ghodsi, Growth, Characterization and Studying of Sol–Gel Derived CdS Nanoscrystalline Thin Films Incorporated in Polyethyleneglycol: Effects of Post-Heat Treatment, Solar Energy Materials & Solar Cells, Vol.105, 2012, pp. 249-262.

[44] L. Gao, Y.-z. Fan, T.-h. Zhang, H.-q. Xu, X.-l. Zeng, T. Hou, W.-c. Dan, J. Zeng, R.-f. An, Biocompatible Carbon-doped MoSe2 Nanoparticles as a Highly Efficient Targeted Agent for Human Renal Cell Carcinoma, RSC Advances, Vol.9, No.20, 2019, pp. 11567-11575.

[45] L. Loghina, M. Chylii, A. Kaderavkova, S. Slang, P. Svec, J. R. Pereira, B. Frumarova, M. Cieslar, M. Vlcek, Highly Efficient and Controllable Methodology of the Cd0.25Zn0.75Se/ZnS Core/Shell Quantum Dots Synthesis, Nanomaterials, Vol.11, No.10, 2021, 2616.

[46] V. V. Ganbavle, G. L. Agawane, A. V. Moholkar, J. H. Kim, K. Y. Rajpure, Structural, Optical, Electrical, and Dielectric Properties of the Spray-Deposited WO3 Thin Films, Journal of Materials Engineering and Performance, Vol.23, No.4, 2014, pp. 1204-1213.

[47] B. J. Cha, T. G. Woo, S. W. Han, S. Saqlain, H. O. Seo, H. K. Cho, J. Y. Kim, Y. D. Kim, Surface Modification of TiO2 for Obtaining High Resistance Against Poisoning during Photocatalytic Decomposition of Toluene, Catalysts, Vol.8, No.11, 2018, 500.

[48] N. Gogurla, A. K. Sinha, S. Santra, S. Manna, S. K. Ray, Multifunctional Au-ZnO Plasmonic Nanostructures for Enhanced UV Photodetector and Room Temperature NO Sensing Devices, Scientific Reports, Vol.4, 2014, Article number: 6483.

[49] H. She, Y. Chen, X. Chen, K. Zhang, Z. Wang, D.-L. Peng, Structure, Optical and Magnetic Properties of Ni@Au and Au@Ni Nanoparticles Synthesized via Non-Aqueous Approaches, Journal of Materials Chemistry, Vol.22, No.6, 2012, pp. 2757-2765.

[50] H. W. Choi, E. J. Kim, S. H. Hahn, Photocatalytic Activity of Au-Buffered WO3 Thin Films Prepared by RF Magnetron Sputtering, Chemical Engineering Journal, Vol.161, No.1-2, 2010, pp. 285-288.

[51] J. Zhao, A. O. Pinchuk, J. M. McMahon, S. Li, L. K. Ausman, A. L. Atkinson, G. C. Schatz, Methods for Describing the Electromagnetic Properties of Silver and Gold Nanoparticles, Accounts of Chemical Research, Vol.41, No.12, 2008, pp. 1710-1720.

[52] M. Zhu, C. M. Aikens, F. J. Hollander, G. C. Schatz, R. Jin, Correlating the Crystal Structure of a Thiol-Protected Au Cluster and Optical Properties, Journal of American Chemical Society, Vol.130, 2008, pp. 5883–5885.

[53] M. Zhu, W. T. Eckenhoff, T. Pintauer, R. Jin, Conversion of Anionic [Au25(SCH2CH2Ph)18]–Cluster to Charge Neutral Cluster via air Oxidation, The Journal of Physical Chemistry C, Vol.112, No.37, 2008, pp. 14221–14224

[54] R. Li, J. Jin, Model Predictions of Toxaphene Degradation in the Atmosphere over North America, Environmental Toxicology and Chemistry, Vol.32, No.12, 2013, pp. 2663–2671.

[55] T. Bartoš, M. Škarek, P. Čupr, P. Kosubová, I. Holoubek, Genotoxic Activity of a Technical Toxaphene Mixture and Its Photodegradation Products in SOS Genotoxicity Tests, Mutation Research/Genetic Toxicology and Environmental Mutagenesis, Vol.565, No.2, 2005, pp. 113-120.

[56] J. Ye, Z. Wan, C. Zhang, L. Zhang, X. Yang, J.-M. Chovelon, L. Zhou, G. Xiu, Novel Insights into the Photochemical Transformation of Neonicotinoid

Insecticides: Potential Involvement of Adjuvants, Journal of Environmental Chemical Engineering, Vol.12, No.5, 2024, 113994.

[57] J. Fenoll, I. Garrido, P. Hellín, P. Flores, S. Navarro, Photodegradation of Neonicotinoid Insecticides in Water by Semiconductor Oxides, Environmental Science and Pollution Research International, Vol.19, 2015, pp. 15055-15066.

[58] M. P. Ormad, N. Miguel, M. Lanao, R. Mosteo, J. L. Ovelleiro, Effect of Application of Ozone and Ozone Combined with Hydrogen Peroxide and Titanium Dioxide in the Removal of Pesticides from Water, Ozone: Science and Engineering, Vol.32, No.1, 2010, pp. 25-32.

[59] J. Araña, C. Garriga i Cabo, C. Fernández Rodríguez, J.A. Herrera Melián, J.A. Ortega Méndez, J.M. Doña Rodríguez, J. Pérez Peña, Combining TiO2-Photocatalysis and Wetland Reactors for the Efficient Treatment of Pesticides, Chemosphere, Vol.71, No.4, 2008, pp. 788-794.

[60] M. Faisal, F. A. Harraz, A. A. Ismail, A. Mohamed El-Toni, S. A. Al-Sayari, A. Al-Hajry, M. S. Al-Assiri, Polythiophene/Mesoporous SrTiO3 Nanocomposites with Enhanced Photocatalytic Activity under Visible Light, Separation Purification Technology, Vol.190, 2018, pp. 33-44.

[61] A. A. Ismail, M. Faisal, A. Al-Haddad, Mesoporous WO3-Graphene Photocatalyst for Photocatalytic Degradation of MB Dye under Visible Light Illumination, Journal of Environmental Sciences, Vol.66, 2018, pp. 328-337.

[62] J. Zhao, A. O. Pinchuk, J. M. McMahon, S. Li, L. K. Ausman, A. L. Atkinson, G. C. Schatz, Methods for Describing the Electromagnetic Properties of Silver and Gold Nanoparticles, Account of Chemical Research, Vol.41, No.12, 2008, pp. 1710-1720.

[63] A. L. Schmucker, N. Harris, M. J. Banholzer, M. G. Blaber, K. D. Osberg, G. C. Schatz, C. A. Mirkin, Correlating Nanorod Structure with Experimentally Measured and Theoretically Predicted Surface Plasmon Sesonance, ACS Nano, Vol.4, No.9, 2010, pp. 5453-5463.

[64] M. V. Dozzi, L. Prati, P. Canton, E. Selli, Effects of Gold Nanoparticles Deposition on the Photocatalytic Activity of Titanium Dioxide under Visible Light, Physical Chemistry Chemical Physics, Vol.11, No.33, 2009, p. 7171-7180.

[65] M. Faisal, J. Ahmed, J. S. Algethami, A. S. Alkorbi, S. A. Alsareii, F. A. Harraz, Ultrafast Removal of Antibiotic Linezolid under Visible Light Irradiation with a Novel Au Nanoparticles Dispersed Polypyrrole-Carbon Black/ZnTiO3 Photocatalyst, Journal of Molecular Liquids, Vol.376, 2023, Article 121499.

[66] D. Channei, K. Chansaenpak, S. Phanichphant, P. Jannoey, W. Khanitchaidecha, A. Nakaruk, Synthesis and Characterization of WO3/CeO2 Heterostructured Nanoparticles for Photodegradation of Indigo Carmine Dye, ACS Omega, Vol.6, No.30, 2021, pp. 19771-19777.

[67] J. Wen, C. Ma, P. Huo, X. Liu, M. Wei, Y. Liu, X. Yao, Z. Ma, Y. Yan, Construction of Vesicle CdSe Nano-Semiconductors Photocatalysts with Improved Photocatalytic Activity: Enhanced Photo Induced Carriers Separation Efficiency and Mechanism Insight, Journal of Environmental Sciences, Vol.60, 2017, pp. 98-107.

[68] N. Nwaji, E. M. Akinoglu, M. Giersig, Gold Nanoparticle-Decorated Bi2S3 Nanorods and Nanoflowers for Photocatalytic Wastewater Treatment, Catalysts, Vol.11, No.3, 2021, 355.

[69] J. Liu, S.-M. Xu, Y. Li, R. Zhang, M. Shao, Facet Engineering of WO3 Arrays toward Highly Efficient and Stable Photoelectrochemical Hydrogen Generation from Natural Seawater, Applied Catalysis B: Environment and Energy, Vol.264, 2019, 118540.

[70] M. Faisal, J. Ahmed, J. S. Algethami, M. Alsaiari, F. A. Harraz, Rapid Elimination of Thiamethoxam Insecticide under Visible Light Using Novel Au Nanoparticles/CdSe/WO3 Ternary Nanocomposite, Journal of Photochemistry and Photobiology A: Chemistry, Vol.447, 2024, 115276.

[71] S. Li, J. Wang, Y. Xia, P. Li, Y. Wu, K. Yang, Y. Song, S. Jiang, T. Zhang, B. Li, Boosted Electron-Transfer by Coupling Ag and Z-Scheme Heterostructures in CdSe-Ag-WO3-Ag for Excellent Photocatalytic H2 Evolution with Simultaneous Degradation,

Chemical Engineering Journal, Vol.417, 2021, 129298.
[72] R. Shi, Y. H. Cao, Y. J. Bao, Y. F. Zhao, G. I. N. Waterhouse, Z. Y. Fang, L. Z. Wu, C. H. Tung, Y. D. Yin,T. R. Zhang, Self-Assembled Au/CdSe Nanocrystal Clusters for Plasmon-Mediated Photocatalytic Hydrogen Evolution, Advanced Materials, Vol.29, 2017, 1700803.
[73] Y. Zhao, K. Jiang, W. Wang, W. Chen, Q. Liu, G. Zhi, Simple Synthesis of Au-WO3 Nanoparticles with Enhanced Photocatalytic Performance, Journal of Electronic Materials, Vol.53, 2024, pp. 4250–4260.
[74] M. Coelhan, M. Maurer, Synthesis of Two Major Toxaphene Components and Their Photostabilities, Journal of Agricultural and Food Chemistry, Vol.53, No.26, 2005, pp. 10105–10112.
[75] E. Kusvuran, D. Yildirim, F. Mavruk, M. Ceyhan, Removal of Chloropyrifos Ethyl, Tetradifon and Chlorothalonil Pesticide Residues from Citrus by Using Ozone, Journal of Hazardous Materials, Vol.241–242, 2012, pp. 287-300.
[76] M. Desseigne, V. Madigou, M.-V. Coulet, O. Heintz, V. Chevallier, M. Arab, Au/WO3 Nanocomposite based Photocatalyst for Enhanced Solar Photocatalytic Activity, Journal of Photochemistry and Photobiology A: Chemistry, Vol.437, 2023, 114427.
[77] T. A. T. Do, T. G. Ho, H. T. Giang, Q. N. Pham, D. T. Nguyen, T. H. L. Nghiem, T. H. Nguyen, M. T. Man, Synthesis of Au-Decorated WO3 Nanoplates for Simultaneous Oxidation of RhB and Reduction of Cr(VI) under Visible Light Irradiation, Vietnam Journal of Chemistry, Vol.62, No.S1: Special Issue: Current Prospects and Challenges in Chemistry (45th Anniversary of the Institute of Chemistry, VAST), Vol.62, 2024, pp. 40-45.

Contribution of Individual Authors to the Creation of a Scientific Article (Ghostwriting Policy)

Prof. Dr. Delia Teresa Sponza and Post-Dr. Rukiye Öztekin took an active role in every stage of the preparation of this article.
The authors equally contributed in the present research, at all stages from the formulation of the problem to the final findings and solution.

Sources of Funding for Research Presented in a Scientific Article or Scientific Article Itself

The experimental phases of this research study were conducted at the National Research Council (NRC) of Canada, Research Centers, Ontario, Canada. The authors would like to thank this body for providing financial support.

Conflict of Interest

The authors have no conflicts of interest to declare that are relevant to the content of this article.

APPENDIX

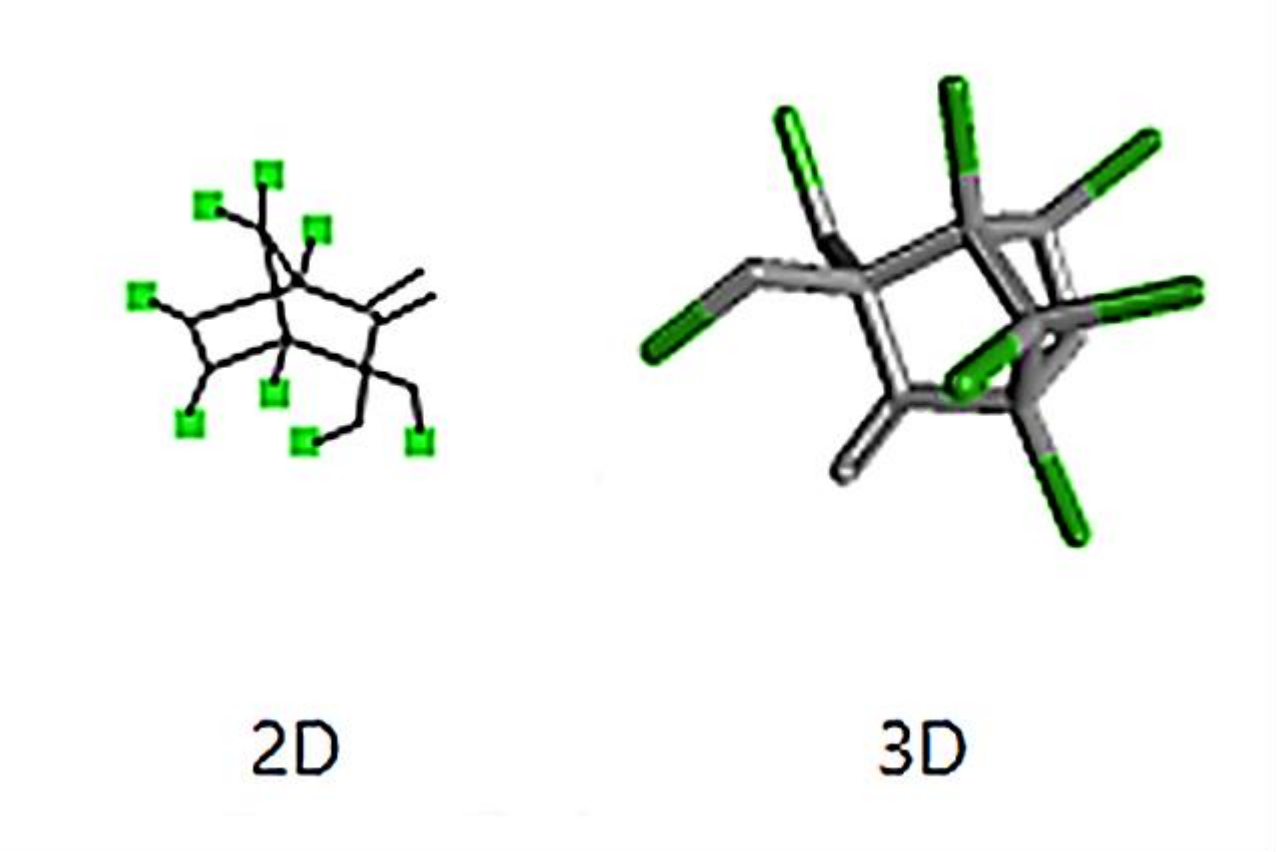

Fig. 1: Chemical structure of Toxaphene

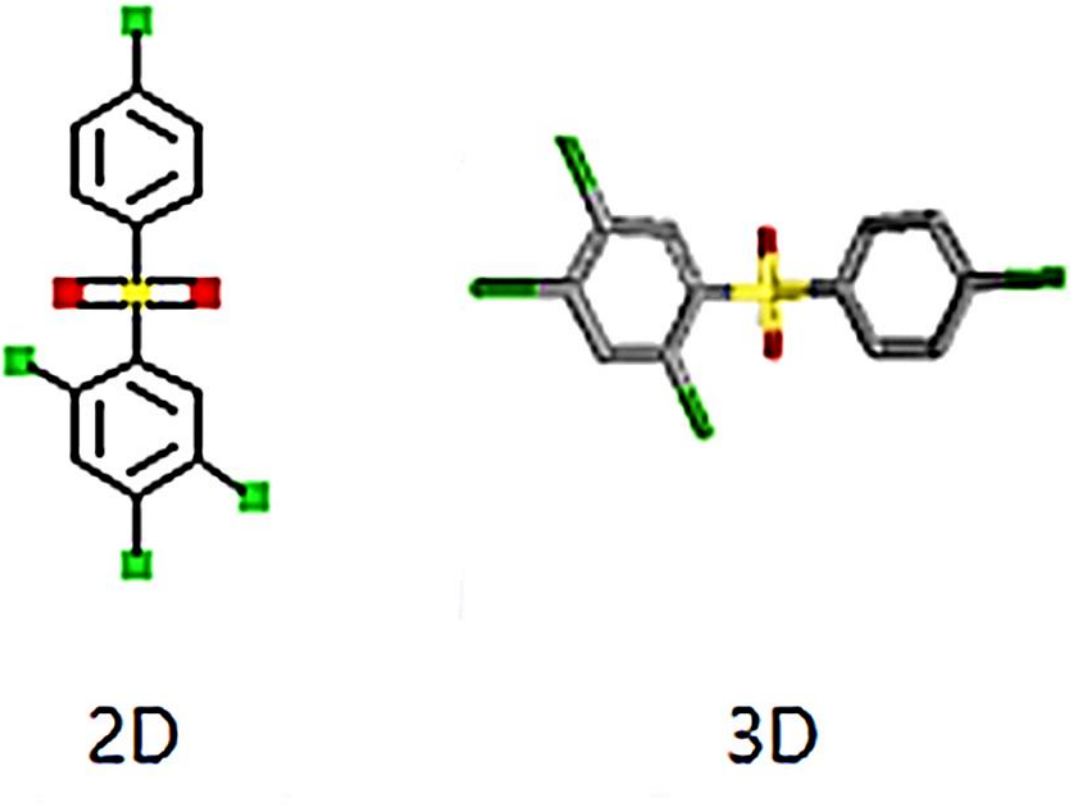

Fig. 2: Chemical structure of Tetradifon

Table 1. Descriptive statistics for toxaphene and tetradifon (mg/l). The number of replicates was (n=3)

Compounds	System	Mean	Std. Dev.	% RSD	Upper 95% Cl	Upper 95% CI
Toxaphene	wastewater	6.99	0.0022	0.013	14.56	2.22
Tetradifon	wastewater	6.98	0.0021	0.012	14.49	2.29

Table 2. Descriptive statistics for e most abundant ions (mg/l) for number of replicates relevant with toxaphene metabolites (n=3)

Ion (m/z)	Name	Mean RA	Std. Dev.	% RSD	Lower 95% Cl	Upper 95% CI
156	1-(3-chlorophenyl) piperazine	1.99	0.0009	0.0001	0.0098	2.89
199	2-endo,3-exo$endo,6-exo,8b,8c,9c,10b,10c nonachlorobomane	2.89	0.00011	0.00011	0.0078	3.98

Table 3. Descriptive statistics for most abundant ions (mg/l) for number of replicates relevant with tetradifon (n=3)

Ion (*m/z*)	Name	Mean RA	Std. Dev.	%RSD	Lower 95% CI	Upper 95% CI
145	2-hydroxy-1-(hydroxymethyl)ethyl ester	1.99	0.0009	0.0001	0.0098	2.89
146	2,3-dihydroxypropyl ester	1.11	0.00012	0.00013	0.00067	2.11
178	1-(hydroxymethyl)-1,2-ethanediyl ester	2.89	0.00011	0.00011	0.0078	3.98

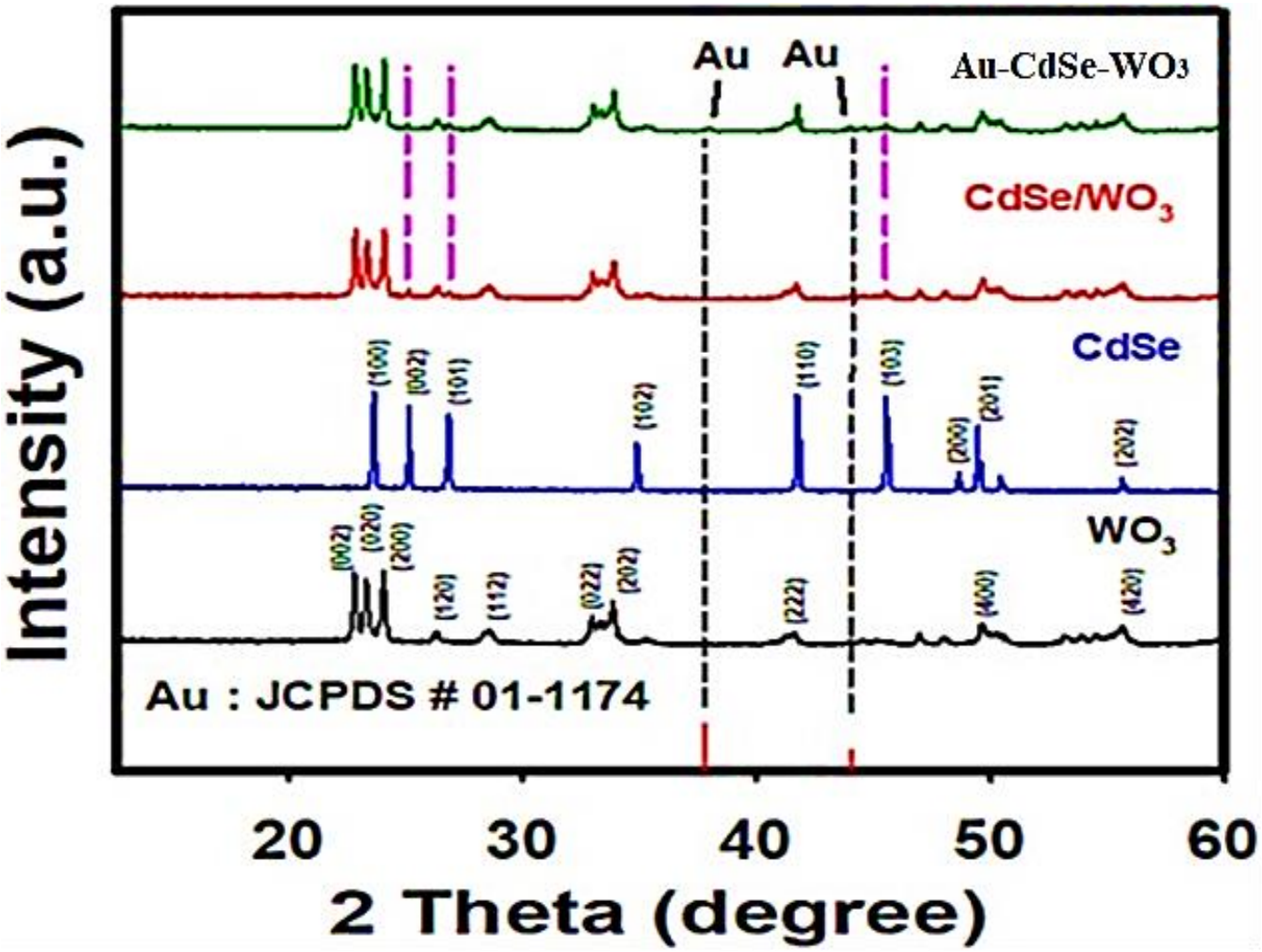

Fig. 3: XRD patterns of WO3, CdSe, CdSe/WO3 and Au/CdSe/WO3 nanocomposites

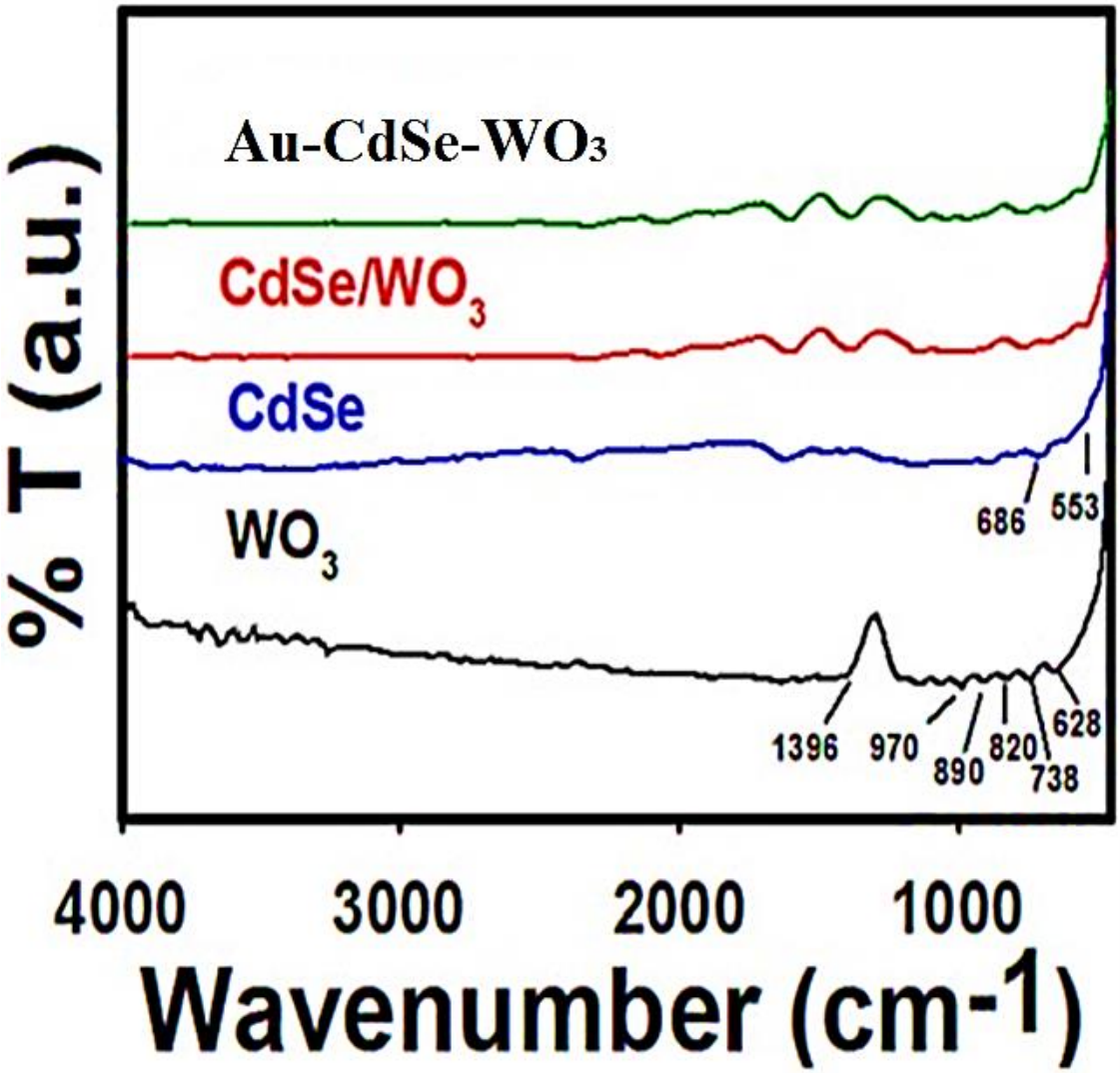

Fig. 4: FTIR analysis of WO3, CdSe, CdSe/WO3 and Au/CdSe/WO3 photocatalysts

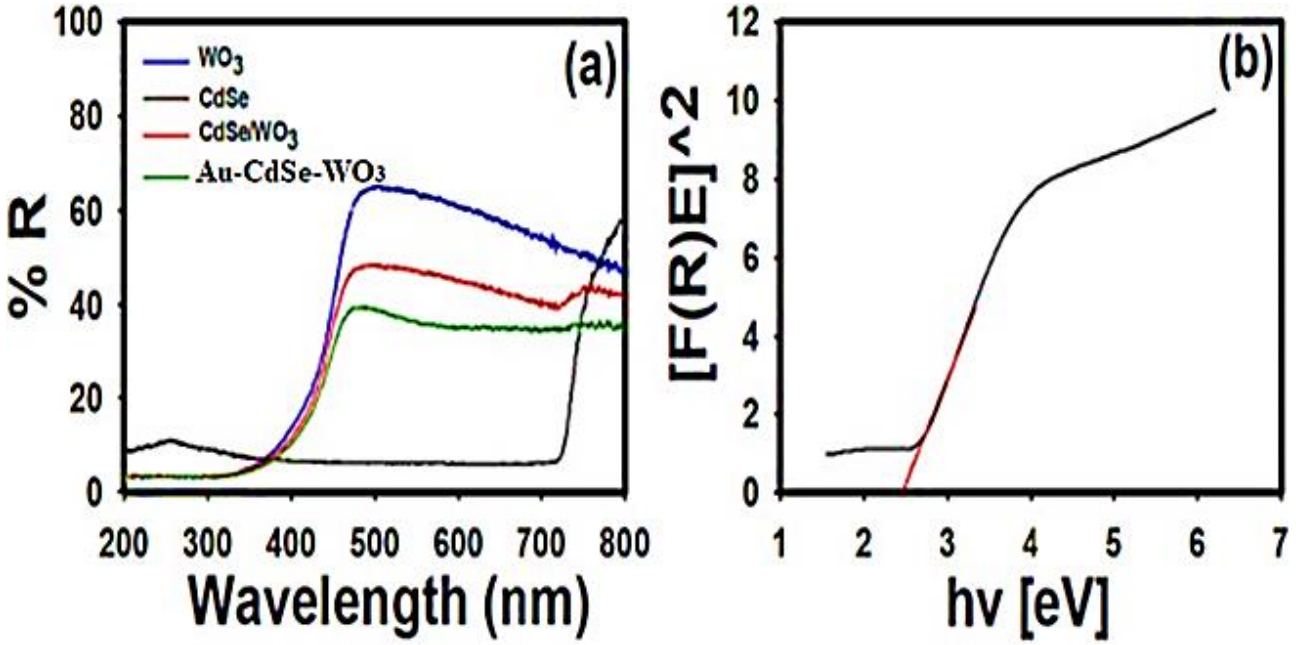

Fig. 5: (a) UV–visible DRS spectra of WO3, CdSe, CdSe/WO3 and Au/CdSe/WO3 photocatalysts and (b) The plot of transferred Kubelka–Munk vs. energy of light absorbed for Au@CdSe/WO3 photocatalyst, respectively

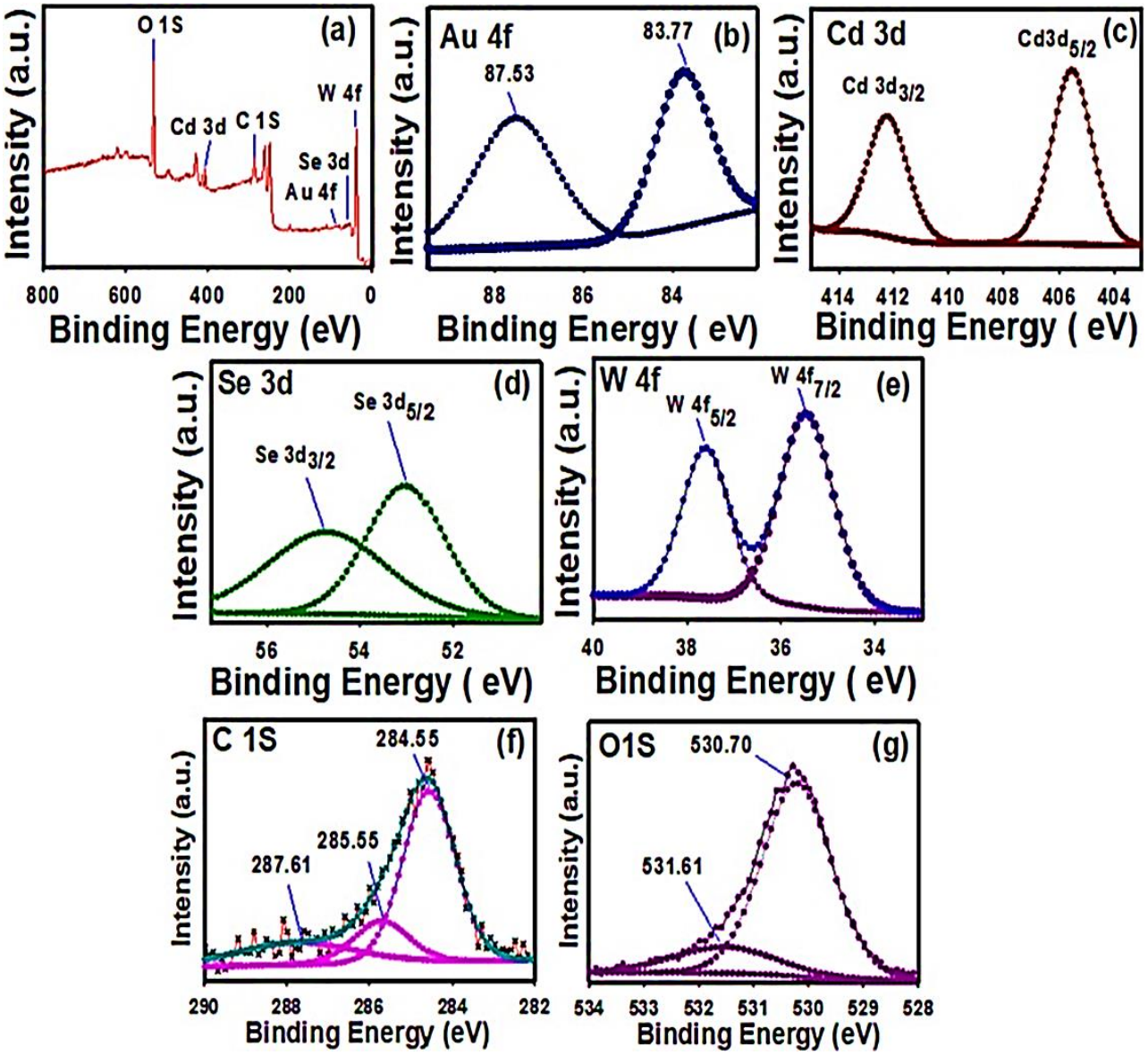

Fig. 6: (a) Wide-scan spectrum and (b-g) narrow-high resolution scan XPS spectra of a u/CdSe/WO3 nanocomposites photocatalyst, respectively. The high-resolution scan spectra were recorded respectively for Au4f, Cd3d, Se3d, W4f, C1s and O1s

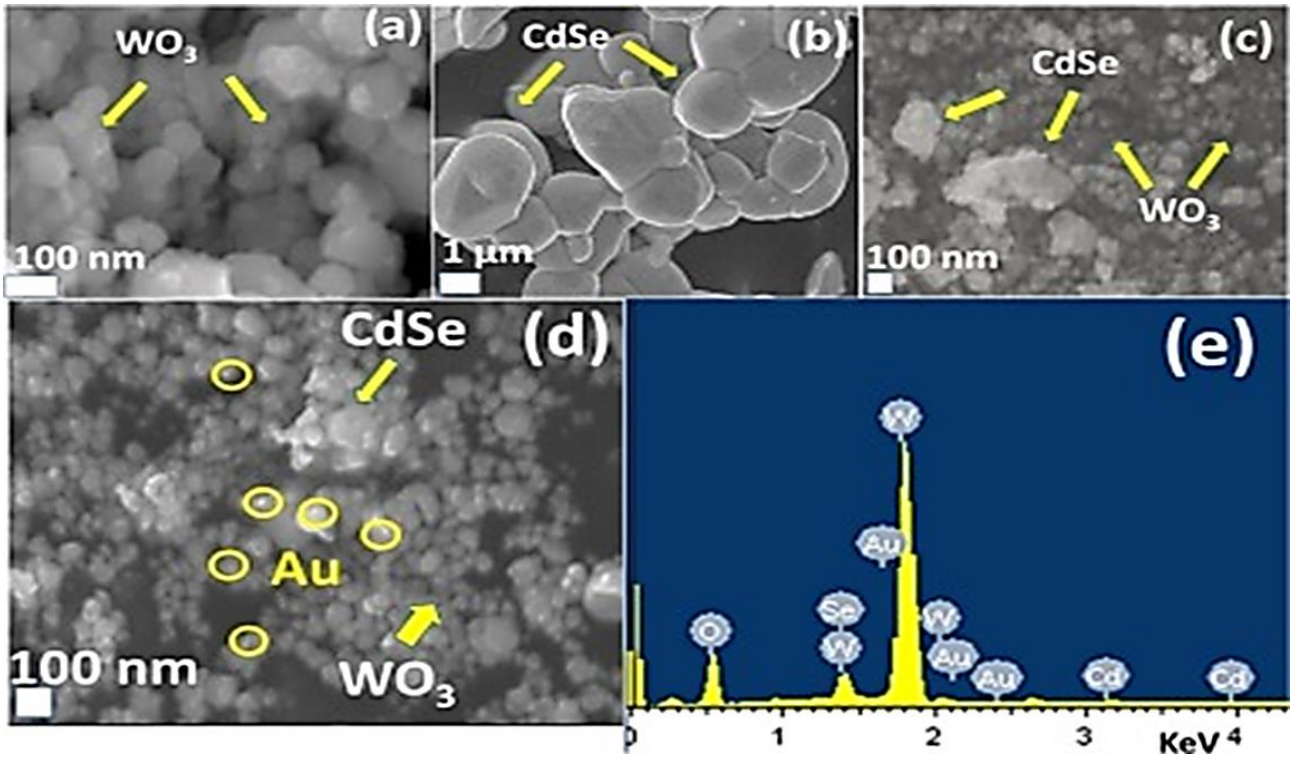

Fig. 7: FESEM images of (a) pure WO3, (b) CdSe, (c) CdSe/WO3, (d) Au/CdSe/WO3 and (e) EDX analysis of a u/CdSe/WO3 photocatalyst, respectively

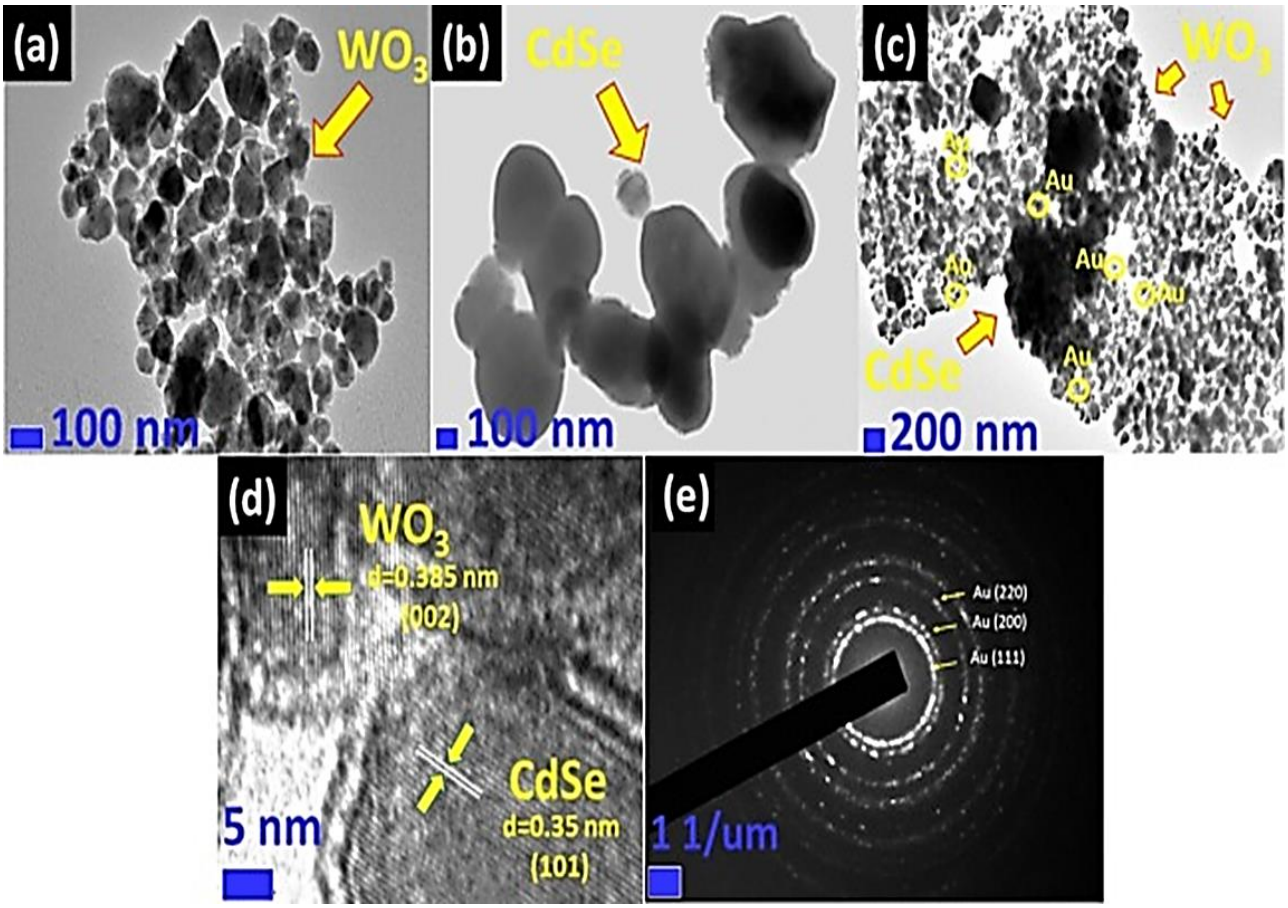

Fig. 8: TEM images of (a) pure WO3, (b) CdSe, (c) Au/CdSe/WO3, (d) HRTEM image of a u@CdSe/WO3 and (e) Selected area electron diffraction pattern of a u/CdSe/WO3, respectively

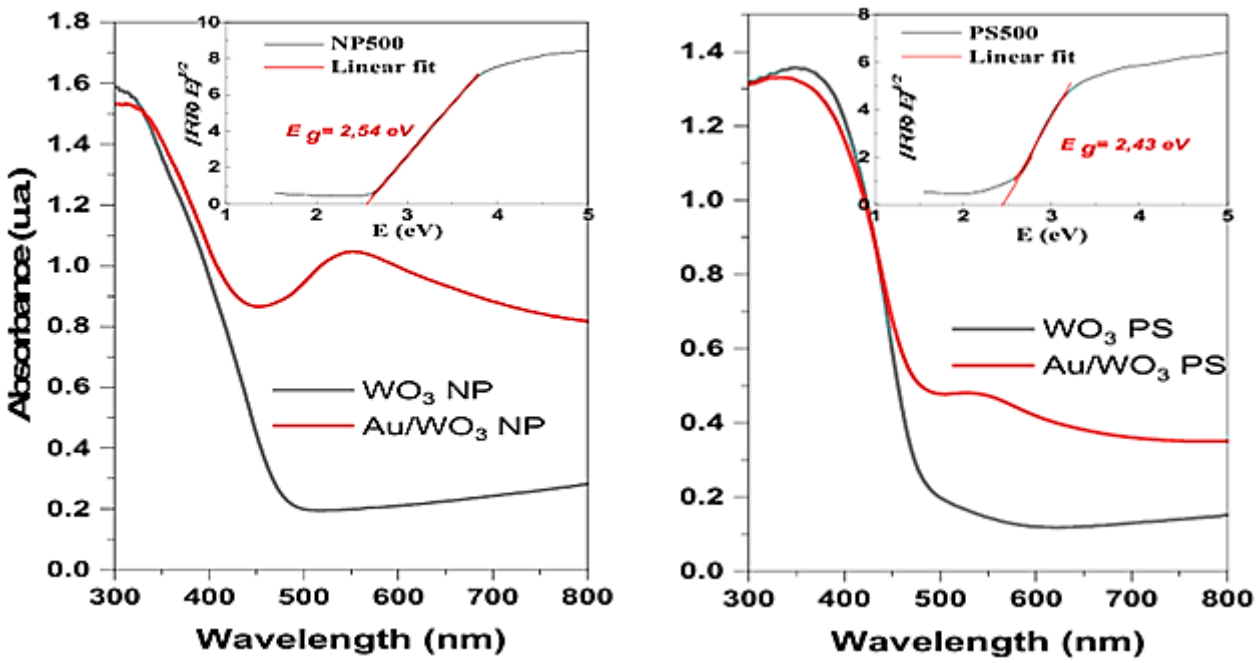

Fig. 9: Comparison of DRS measurements in the visible UV range for the materials before (black lines) and after (red lines) Au grafting onto (a) WO3 NP and (b) WO3 PS supports, respectively. Insert figures correspond to the Kubelka–Munk plots

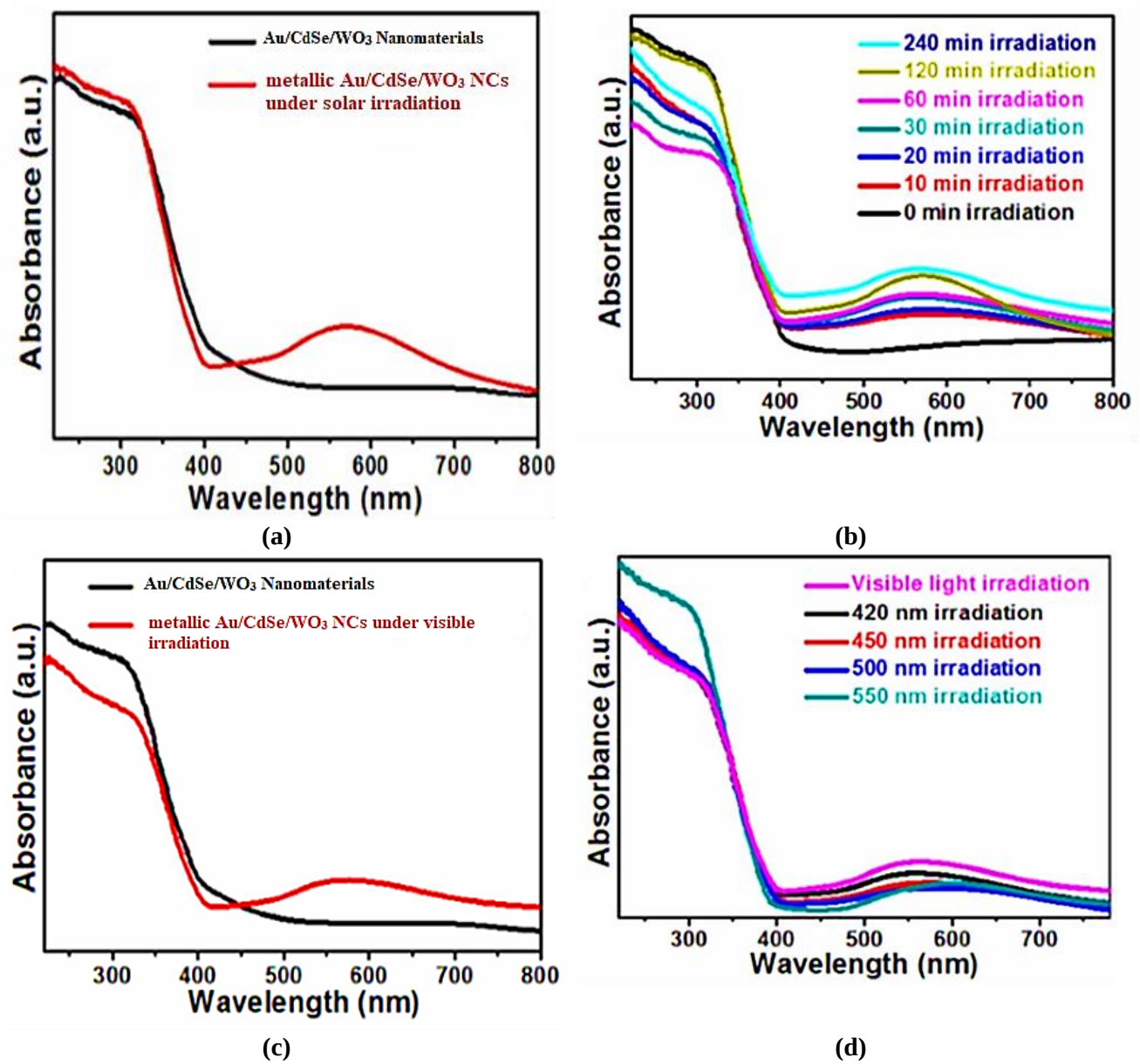

Fig. 10: UV-visible DRS analysis of a u/CdSe/WO3 nanomaterials and metallic Au/CdSe/WO3 nanocomposites (a) under solar irradiation, (b) versus solar irradiation times, (c) under visible irradiation, and (d) versus visible light irradiations, respectively

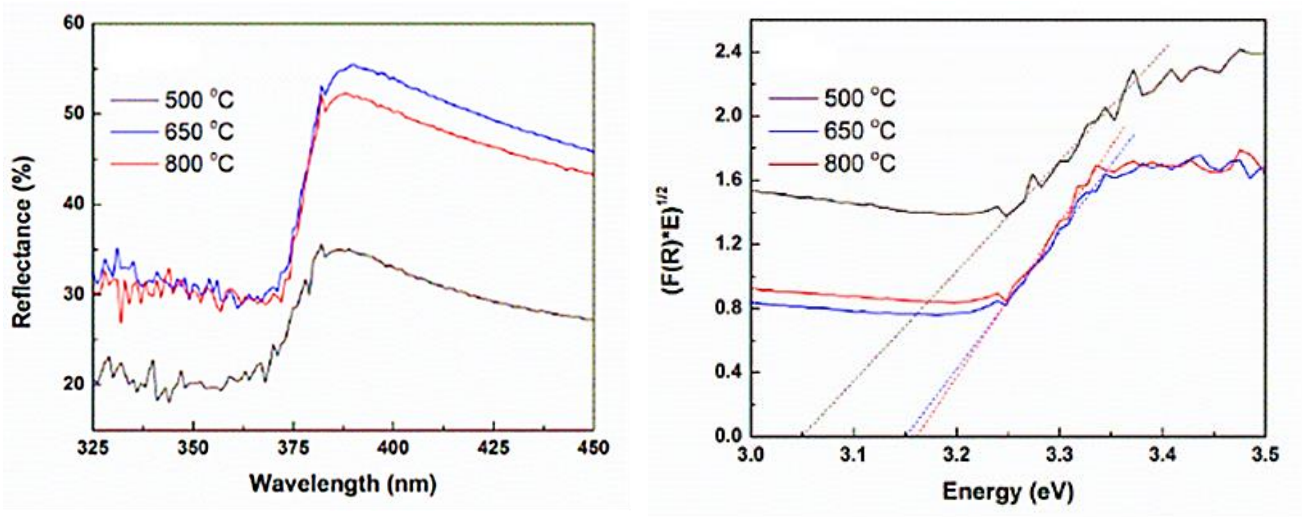

Fig. 11: Reflectance spectra (a) and Kubelka-Munk functions, (b) for Au/Cd/Se/ WO3 nanocomposites calcined at different temperatures

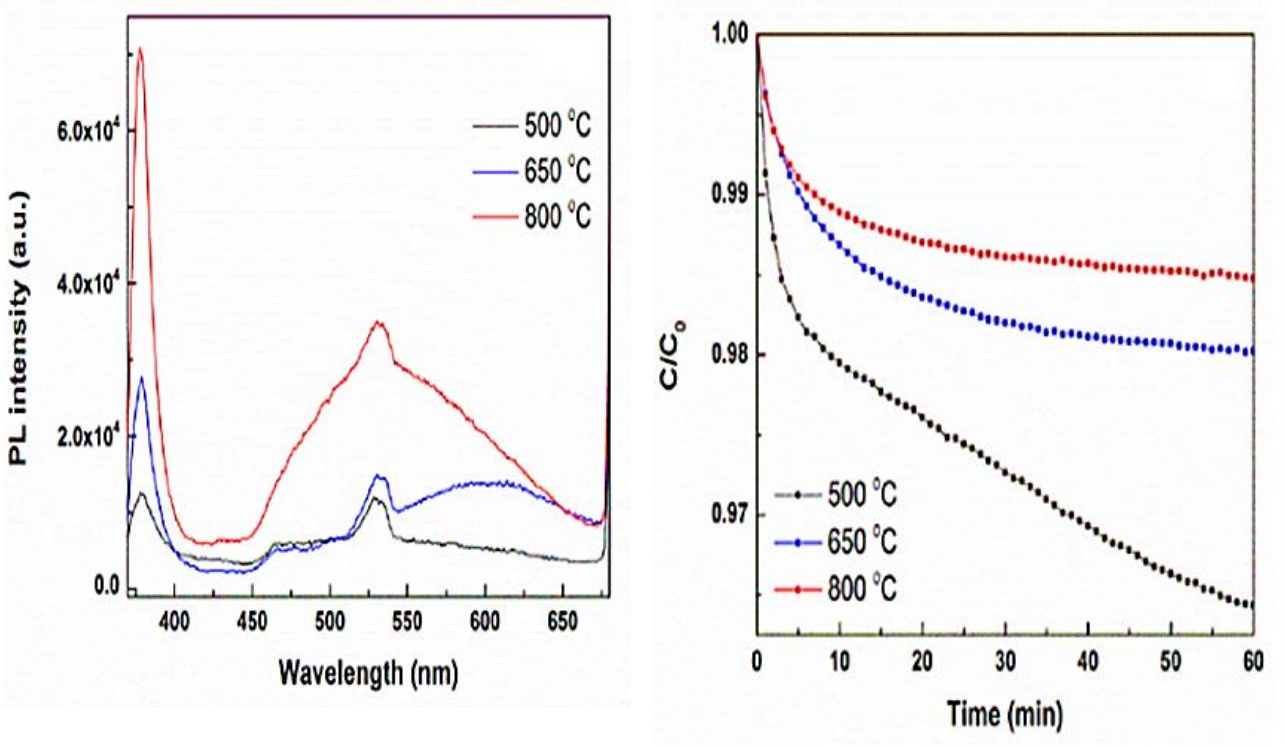

(a) **(b)**

Fig. 12: (a) PL spectra of a u/Cd/Se/ WO3 nanocomposite (b) photocatalytic degradation curves of tetradifon under UV irradiation calcined at different temperatures, respectively

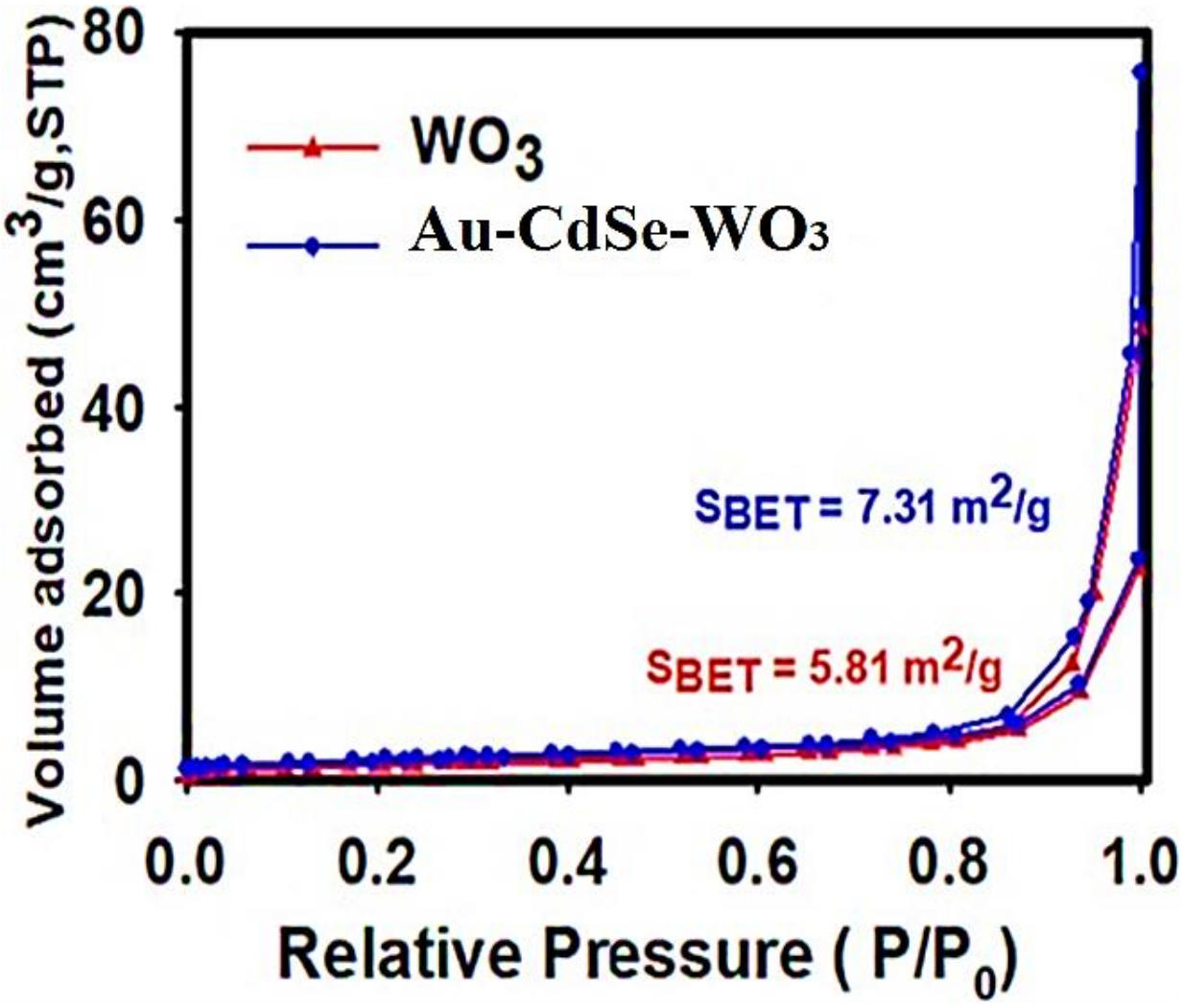

Fig. 13: N2 sorption isotherm for pure WO3 and Au/CdSe/WO3 photocatalyst

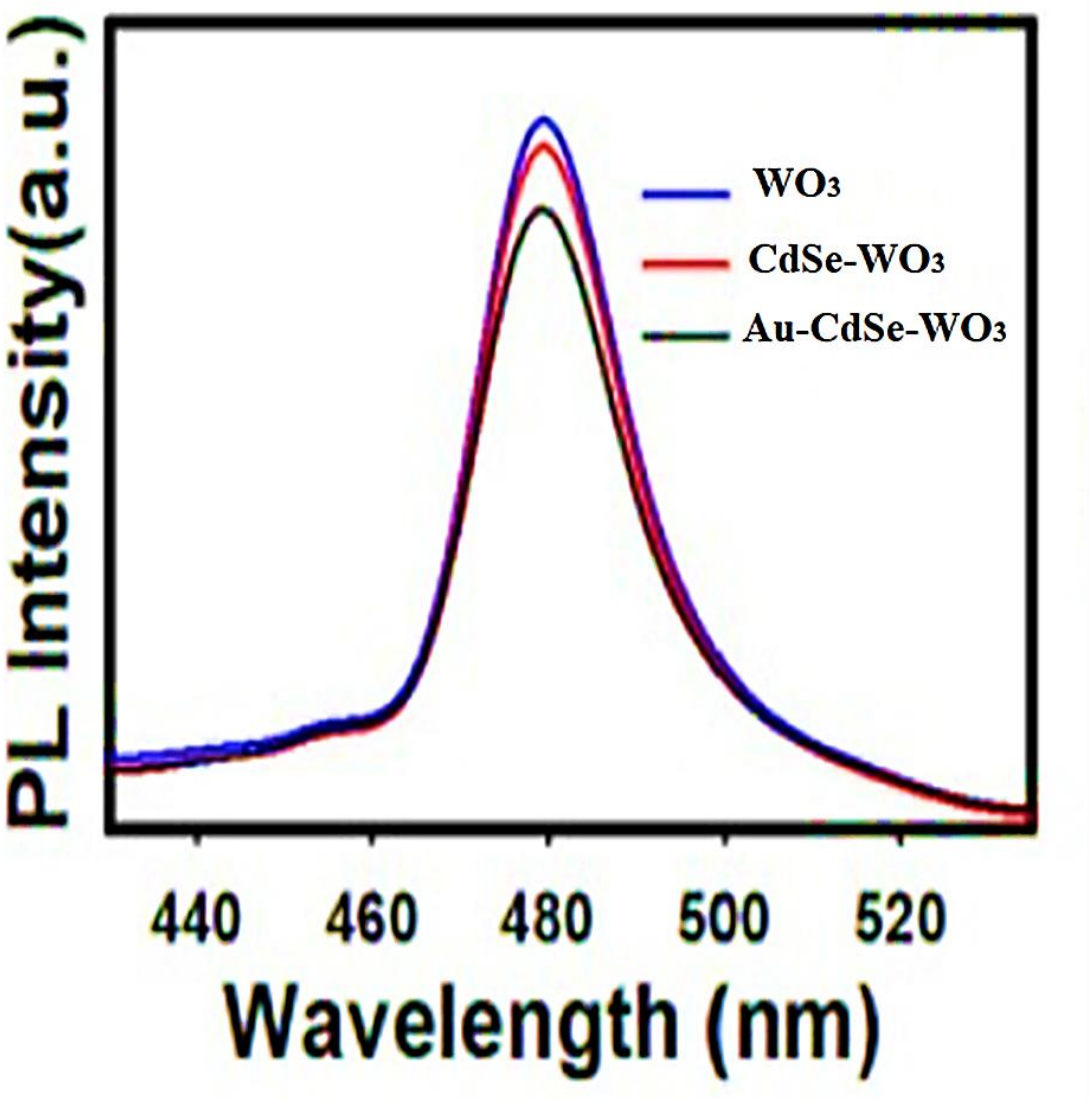

Fig. 14: PL spectra of WO3, CdSe/WO3 and Au@CdSe/WO3 nanocomposites (excited at λ = 328.99 nm)

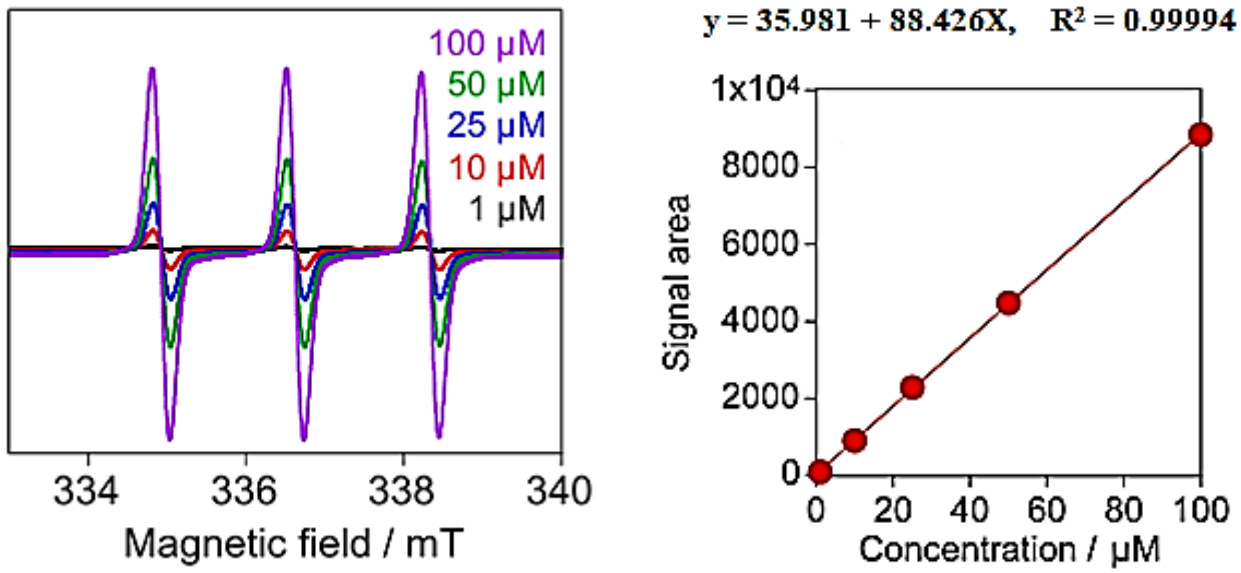

(a) **(b)**

Fig. 15: (a) ESR spectra of a u@CdSe/WO3 NCs (aN=1.7 mT, g=2.0057), and (b) Calibration curve of a u@CdSe/WO3 nanocomposites concentration versus ESR signal area, respectively

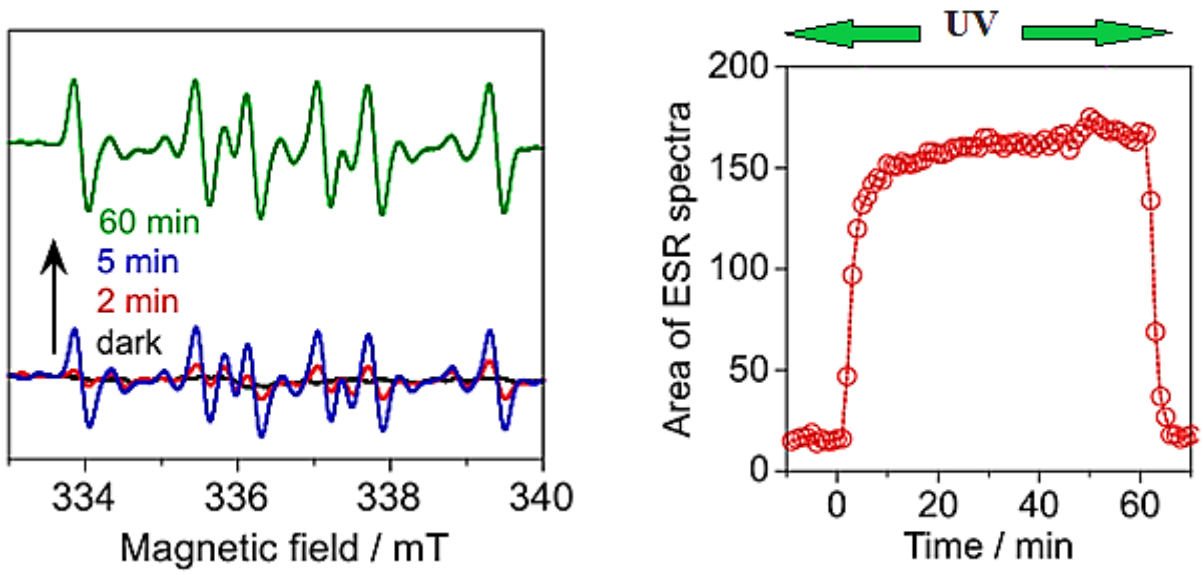

(a) **(b)**

Fig. 16: Continuous-flow ESR measurements for the photoanodic reaction with 10 vol% methanol over a WO3 photoanode at 1.2 V vs. RHE under 365 nm UV light (10 mW/cm2) for 60 min. (a) ESR spectra of the electrolyte solution as a function of PEC reaction time, and (b) Time course of the ESR peak area, respectively

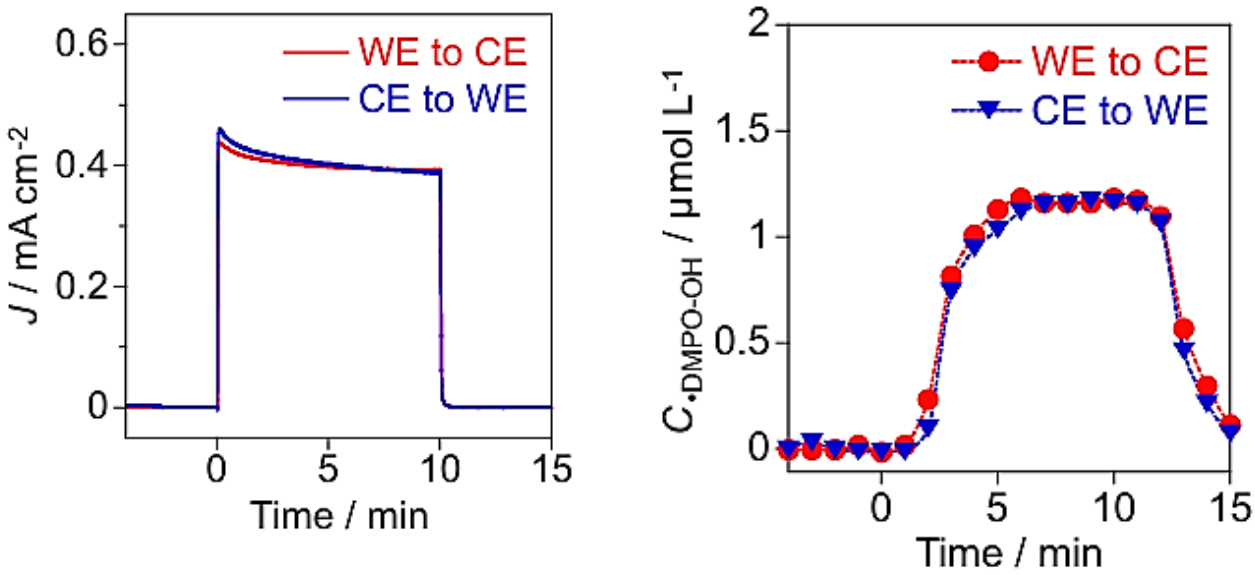

(a) **(b)**

Fig. 17: Effect of flow direction through the cell electrodes on (a) current density and (b) OH● radical concentration for WO3 photoanode at 1.20 V vs. RHE under 365 nm UV light (10 mW/cm2) for 10 min, respectively

Table 4. Effect of increasing Au/CdSe/WO3 nanocomposites concentrations on photodegradation yields of insecticides, (n=3, mean values, SD: standard deviation)

Au/CdSe/WO_3 Nanocomposites Concentration (mg/l)	**Toxaphene Removal Efficiency (%) ± SD**	**Tetradifon Removal Efficiency (%) ± SD**
0.5	45 ± 0.0010	40 ± 0.0010
1.0	99 ± 0.0011	97 ± 0.0011
1.5	96 ± 0.0010	92 ± 0.0010
2.0	90 ± 0.0011	88 ± 0.0011

Table 5. Effect of increasing times on photodegradation yields of insecticides, (n=3, mean values, SD: standard deviation)

Time (min)	**Toxaphene Removal Efficiency (%) ± SD**	**Tetradifon Removal Efficiency (%) ± SD**
5	45 ± 0.0010	40 ± 0.0011
10	99 ± 0.0011	97 ± 0.0010
15	90 ± 0.0012	87 ± 0.0011
20	80 ± 0.0010	75 ± 0.0012

Table 6. Effect of of pH on photodegradation yields of insecticides, (n=3, mean values, SD: standard deviation)

pH	**Toxaphene Removal Efficiency (%) ± SD**	**Tetradifon Removal Efficiency (%) ± SD**
5	45 ± 0.0012	40 ± 0.0013
7	76 ± 0.0010	73 ± 0.0012
8	99 ± 0.0011	97 ± 0.0010
10	40 ± 0.0010	35 ± 0.0010

Table 7. Effect of light power on photodegradation yields of insecticides, (n=3, mean values, SD: standard deviation)

Light Power (W/m^2)	**Toxaphene Removal Efficiency (%) ± SD**	**Tetradifon Removal Effiency (%) ± SD**
10	59 ± 0.0012	56 ± 0.0010
20	99 ± 0.0009	97 ± 0.0009
30	72 ± 0.0009	70 ± 0.0011
40	50 ± 0.0012	45 ± 0.0012

Table 8. Effect of insecticide concentrations and temperature on insecticides photodegradation yields, (n=3, mean values, SD: standard deviation)

Toxaphene/ Tetradifon Concentration (mg/l)	**Temperature (ºC)**	**Toxaphene Removal Efficiency (%) ± SD**	**Tetradifon Removal Efficiency (%) ± SD**
100	20	59 ± 0.0010	56 ± 0.0010
300	40	99 ± 0.0002	98 ± 0.0003
800	50	99 ± 0.0001	97 ± 0.0010
1000	60	96 ± 0.0010	96 ± 0.0012

Table 9. Reusability of Au/CdSe/WO3 NCs during photodegradation of toxaphene and tetradifon insecticides

Run	Toxaphene Photodegradation Yield (%)	Tetradifon Photodegradation Yield (%)
1	99	99
2	99	99
3	99	99
4	99	99
5	99	99
……	99	99
……	99	99
60	99	99
61	99	99
62	99	99
63	99	99
…..	99	99
…..	99	99
80	98	98